FRONT MATTER

Title

Past terrestrial hydroclimate driven by Earth System Feedbacks

Authors

R. Feng[1*], T. Bhattacharya[2], B. Otto-Bliesner[3], E. Brady[3], A. Haywood[4], J. Tindall[4], S. Hunter[4], A. Abe- Ouchi[5], W. -L. Chan[5], M. Kageyama[6], C. Contoux[6], C. Guo[7], X. Li[8], G. Lohmann[9], C. Stepanek[9], N. Tan[10], Q. Zhang[11], Z. Zhang[8], Z. Han[12], J. R. Williams[13], D. J. Lunt[13], H. Dowsett[14]

Affiliations

1. Department of Geosciences, College of Liberal Arts and Sciences, University of Connecticut, Connecticut, USA
2. Department of Earth and Environmental Sciences, Syracuse University
3. Climate and Global Dynamics Laboratory, National Center for Atmospheric Research, Boulder, Colorado, USA
4. School of Earth and Environment, University of Leeds, Woodhouse Lane, Leeds, West Yorkshire, LS29JT, UK
5. Atmosphere and Ocean Research Institute, University of Tokyo, Kashiwa, Japan.
6. Laboratoire des Sciences du Climat et de l'Environnement, LSCE/IPSL, CEA-CNRS-UVSQ, Université Paris-Saclay, F-91191 Gif-sur-Yvette, France
7. NORCE Norwegian Research Centre, Bjerknes Centre for Climate Research, 5007 Bergen, Norway
8. Department of Atmospheric Science, School of Environmental studies, China University of Geoscience, Wuhan, 430074, China
9. Alfred Wegener Institute-Helmholtz Centre for Polar and Marine Research, Bremerhaven, Germany
10. Key Laboratory of Cenozoic Geology and Environment, Institute of Geology and Geophysics, Chinese Academy of Sciences, Beijing 100029, China
11. Department of Physical Geography and Bolin Centre for Climate Research, Stockholm University, Stockholm, Sweden
12. College of Oceanography/Key Laboratory of Marine Hazards Forecasting, Ministry of Natural Resources/Key Laboratory of Ministry of Education for Coastal Disaster and Protection, Hohai University, Nanjing, China
13. School of Geographical Sciences and Cabot Institute, University of Bristol, University Road, Bristol, BS8 1SS, UK
14. Florence Bascom Geoscience Center, U. S. Geological Survey, Reston, Virginia, USA

*Corresponding author. Email: ran.feng@uconn.edu

None-peer-reviewed preprint submitted to EarthArXiv

Currently in review

Submitted to Science Advances – 31 May 2021

Abstract

Geologic evidence suggests drastic reorganizations of subtropical terrestrial hydroclimate during past warm intervals, including the mid-Piacenzian Warm Period (MP, 3.3 to 3.0 Ma). Despite having a similar to present-day atmospheric CO_2 level (pCO_2), MP featured moist subtropical conditions with high lake levels in Northern Africa, and mesic vegetation and sedimentary facies in subtropical Eurasia. Here, we demonstrate that major loss of the northern high-latitude ice sheets and continental greening, not the pCO_2 forcing, are key to generating moist terrestrial conditions in subtropical Sahel and east Asia. In contrast to previous hypotheses, the moist conditions simulated in both regions are a product of enhanced tropospheric humidity and a stationary wave response to the surface warming pattern, both varying strongly in response to land cover changes. These results suggest that past terrestrial hydroclimate states were driven by Earth System Feedbacks, which may outweigh the direct effect of pCO_2 forcing.

Teaser

Earth System Feedbacks may outweigh the direct effect of pCO_2 forcing in driving past hydroclimate state.

Introduction

Geologic evidence suggests dramatic reorganizations of subtropical climate during past greenhouse climate intervals, including the mid-Piacenzian Warm Period (3.3 to 3.0 Ma, MP for short). Multiple proxies of hydroclimate indicate large, deep lakes and reduced dust flux across north Africa(*1*, *2*). There is also evidence for more mesic vegetation in South and East Asia(*3*, *4*). Moreover, proxies generally suggest significant regions of subtropical Eurasia were wetter prior to the onset of northern hemisphere glaciation. These changes, which imply large increases in precipitation minus evaporation (P-E), are associated with $p\mathrm{CO_2}$ levels of approximately 400 ppm (*5*, *6*). Moderate increase of precipitation across these regions may be expected due to tropospheric moistening(*7*), enhanced land-sea thermal contrast(*8*), and enhanced inland moisture advection and ventilation(*9*, *10*). However, evaporation also increases in response to surface warming. As a result, predicted changes in terrestrial water balance (P-E) remain equivocal across broad subtropical continents(*11*).

Model predicted response of terrestrial hydroclimate to CO_2 increase broadly follows the “wet-gets-wetter, dry-gets-drier” paradigm(*7*) with strong modulations from land warming pattern, land-sea warming contrast(*12*), tropical SST pattern(*13*), and feedbacks from soil moisture and CO_2 fertilization effects on leaf phenology(*14*, *15*). The net effect of these mechanisms potentially results in muted changes in P-E in subtropical Sahel and east Asia seen in simulations featuring middle of the road future warming scenarios, such as the Shared Socioeconomic Pathways (SSP245) (Fig. 1a and d). These future scenarios are often thought to be comparable to the MP climate(*16*, *17*) (Fig. 1a). The disparity between hydroclimate state recorded by MP proxies and future simulations challenges our understanding of terrestrial hydroclimate sensitivity to CO_2 radiative forcing.

Two leading hypotheses might explain the wetter subtropical continents during past warm climates. One emphasizes the hydroclimate impact of an El Niño-like Pacific mean state. SST records from the tropical Pacific record greater warming across the eastern equatorial Pacific than the western Pacific warm pool (*18-22*), resulting in an El-Niño-like pattern of SST anomalies. An El Niño-like tropical Pacific SST pattern may strengthen and shift the subtropical jet equatorward, enhancing the transient eddy-driven moisture convergence and ascent(*23*, *24*). The other hypothesis focuses on the role of a sluggish Hadley Circulation (HC) that is inferred from a relaxed meridional SST gradient(*25-27*). A weaker HC may result in weakened zonal mean moisture divergence from the subtropics and, in turn, reduced aridity(*28-30*).

Here, using atmosphere-ocean coupled global climate model (GCM) simulations from the Pliocene Model Intercomparison Project Phase II (PlioMIP2) (*31-33*), we assess whether the current generation ESMs can reproduce the pattern of MP hydroclimate suggested by proxies. We further develop several new simulations using the Community Earth System Model version 2(*34*, *35*) to explore the extent to which simulated MP hydroclimate changes across Sahel and subtropical Asia East Asia can be generated by changes in CO_2 radiative forcing, tectonics, or vegetation and ice sheets. In contrast to previous hypotheses, simulated Pliocene hydroclimate conditions are driven by tropospheric moistening, and changes to stationary wave dynamics. Model skills at simulating Pliocene hydroclimate states strongly scale with Earth System Sensitivities of individual models instead of the Equilibrium Climate Sensitivities. Our results highlight the importance of Earth System Feedbacks in driving past hydroclimate, which may outweigh the direct effect of CO_2 forcing.

Results

P-E pattern in models and proxies

MP changes in precipitation minus evaporation (δ(P-E)) and other climate variables are calculated with respect to preindustrial (PI) values. The last 100 years of simulations by 13 PlioMIP2 ESMs were averaged to produce the ensemble mean (Table S1). A robust moistening signal that is larger than internal variability of individual models is found across the Sahel and subtropical Eurasia (Fig. 1b). This pattern is the most pronounced during the boreal summer months (June to September) (Fig. 1c) with little or compensating changes during the winter months (December to March) (Fig. S1). The spatial continuity of positive δ(P-E) from North Africa to subtropical eastern Asia is not a visual coincidence: models that show a small precipitation increase in the Sahel also tend to show a small increase in the southeast Asia (Fig. 1d), suggesting similar processes driving hydroclimate changes in both regions, which is later confirmed by the moisture budget analysis.

To compare modeled patterns of hydroclimate change to available geologic data, we compiled proxy indicators of MP terrestrial hydroclimate, drawing on existing compilations(*30*, *36*, *37*) as well as our own literature search. We identify a total of 64 proxy records that include sedimentological indicators, palynological, floral or faunal, offshore marine records, and stable isotope analyses of organic and inorganic materials (see Methods) (Fig. S2). These records are most appropriately interpreted as qualitative or semi-quantitative indicators of hydroclimate. We therefore quantify the extent to which proxies and models produce the same patterns of wetter, drier, or unchanged MP hydroclimate changes using a metric known as Gwet’s AC designed for categorical data (See Methods). To account for different biases in climatological rainfall across models, model values of P-E are expressed as % changes from pre-industrial values.

The annual patterns of δ(P-E) revealed by the PlioMIP2 ensemble are consistent with proxy indicators of hydroclimate across Sahel and subtropical Eurasia (Fig. 2), and are strongly driven by the summer δ(P-E) patterns (Fig. S3). Yet, different models show varying skill at capturing the pattern in the proxy records (Figs. 2a and S4). For instance, IPSL-CM6, and EC-Earth3.3, two models with the highest level of agreement between MP proxies and simulations, show expansive inland wetter conditions across North Africa, the Mediterranean, and subtropical Asia (Figure S4). In contrast, NorESM-L and GISS-E2-1-G, two of the models with the lowest proxy-model agreement, show highly mixed or muted δ(P-E) across this region (Fig. S4). Despite intermodal spread in the degree of proxy-model agreement, the majority of models, and the multi-model mean, show statistically significant proxy-model agreement at δ(P-E) threshold of 20% above the PI (Fig. S4). While we analyze proxy-model agreement based on annually averaged δ(P-E) in models, intermodal spread in the fit between proxy and model is strongly driven by the summer signal (Fig. 2c).

CO_2 or boundary conditions in driving positive δ(P-E)

Three sets of simulations are constructed with the Community Earth System Model version 2 (CESM2)(*38*) to quantify contributions to δ(P-E) from the following forcings: 400 ppm CO_2 (F_{CO2}), changes in biome distribution and ice sheets (F_{vegice}), and geography and topography (F_{geotop}). Separation of F_{vegice} and F_{CO2} is designed to separate vegetation and ice sheet responses from the direct responses to CO_2 forcing. The former represents Earth System Feedbacks, which are not typically considered when evaluating equilibrium climate responses to CO_2 forcing(*39*).

F_{vegice} explains 68% of the mean δ(P-E) in the full forcing (F_{all}) CESM2 experiment across subtropical Sahel and east Asia, while contributions from F_{CO2} and F_{geotop} are small (Fig. 3a – d). Furthermore, only F_{vegice} produces a similar level of proxy-model agreement compared to the F_{all}. Both F_{CO2} and combined $F_{geotopo}$ and F_{CO2} produce low values of Gwet's AC (Fig. 2b). These results suggest that F_{vegice}, not F_{CO2}, is key to generating moist climate across both regions.

Compared to F_{all}, F_{vegice} accounts for ~50% increase of global mean surface temperature (2.7°C), and 58% increase (0.45 g/kg) of global mean tropospheric (100 to 1000 hPa) specific humidity. In the Northern subtropics (20°N and 30°N), F_{vegice} explains an even greater fraction of tropospheric moistening (61%, or 0.56 g/kg). In contrast, F_{CO2} accounts for 45% of global mean surface warming (2.4°C), 31% (0.24 g/kg) of global mean tropospheric moistening, but only 26% of tropospheric moistening in the northern subtropics. F_{geotop} has much smaller influences on temperature and moisture responses globally. The influence of F_{geotop} is slightly elevated in the northern subtropics accounting for 13% increase (0.11 g/kg) in tropospheric humidity. Warming due to F_{vegice} is attributable to both lowered surface albedo, and enhanced evapotranspiration. Areas where boreal forest shifts and expands northward, and where mid-latitude deserts becomes vegetated feature substantially lowered surface albedo (Fig. 3c). New territories of boreal forests also show large increases of upward latent heat flux, suggesting enhanced water vapor feedback(*40*) (Fig. 3b). Similar increase in latent heat flux also occurs in the northern subtropics where δ(P-E) is positive, contributing to enhanced tropospheric humidity and warming.

Dynamical linkage between climate forcing conditions and MP hydroclimate

In order to identify the dynamical linkage between climate forcing conditions and hydroclimate in subtropical Sahel and east Asia, we adapt the published moisture budget diagnostics (MBD) (*41*) to decompose simulated June to September δ(P-E) by individual models (Methods) into changes in seasonal cycle of tropospheric moisture content ($δ(P\text{-}E)_t$), changes in zonal mean circulation dynamics ($δ(P\text{-}E)_{[V]}$) and stationary wave dynamics ($δ(P\text{-}E)_{V*}$) (Fig. 4a and 4b), changes in tropospheric moisture content ($δ(P\text{-}E)_Q$) (Fig. 4c), changes in interactions between moisture and airflow dynamics $δ(P\text{-}E)_{VQ}$, and a residual term ($δ(P\text{-}E)_{Resi}$) (Fig. 4d). Stationary wave is quantified as the temporal mean departure from the zonal mean following the classic circulation decomposition(*42*). The residual term combines effects of high frequency variability of transient eddies and changes of topography (see Methods).

The MBD results are consistent among PlioMIP2 ensemble mean and F_{vegice}, suggesting common mechanisms for δ(P-E) among these two sets of experiments (Fig. 4e and f, and Fig. S5). As revealed by MBD, contributions from both $δ(P\text{-}E)_t$ and $δ(P\text{-}E)_{VQ}$ are insignificant in both regions (Fig. S5). Noticeably, both $δ(P\text{-}E)_{[V]}$ and $δ(P\text{-}E)_{Resi}$ are also small (Fig. 4a and d). A small $δ(P\text{-}E)_{[V]}$ suggests little contribution from changes in the zonal mean HC to δ(P-E). This inference is also supported by δ(P-E) pattern shown in Fig. 1b. Coherent δ(P-E) between 0 and 30°N is expected across all longitudes if zonal mean HC was the primary driver, similar to what is demonstrated in the previous study(*30*). However, this is not the case. Positive δ(P-E) displays a clear latitudinal offset between land and ocean, and between subtropical east Asia and North American continents.

A small $δ(P\text{-}E)_{Resi}$ suggests that the net influence from changes of transient eddies and topography is small (Fig. 4d). In PlioMIP2 experiments, storm track activities and subtropical jet stream in the Northern Hemisphere both weaken as shown by the 850 hPa eddy kinetic energy (EKE) and 200 hPa zonal wind speed (Fig. S6a and b). These responses are opposite to the expected responses to El Niño-like SSTs (*24*), and likely driven by other aspects of simulated climate change such as Arctic amplification(*43*). Moreover, if the El Niño-like SST is key to driving the ensemble mean δ(P-E), negative δ(P-E) in the northern Africa paired with positive δ(P-E) in the southeast Asia are expected as part of the fingerprints of tropospheric teleconnection(*44*), which is not seen in the simulated MP δ(P-E) (Fig. 1b).

Positive δ(P-E) in the subtropical Sahel and subtropical Asia primarily arises from changes in stationary wave dynamics ($\delta(P\text{-}E)_{V^*}$) (Fig. 2b) and increased zonal mean moisture content ($\delta(P\text{-}E)_{[Q]}$). Changes in stationary wave is further decomposed into components associated with different wave numbers through Fourier decomposition of stream function (SF) anomalies at 600 hPa. The SF anomalies are calculated as departures from the zonal mean and reference state (Method) (Fig. 3d - f). As shown by the Fourier decomposition, wave number 1 (wave-1) of SF anomalies accounts for 67% of the total wave energy between 0 – 90°N. This wave component features cyclones separately centered in the western Europe and North Africa, and anticyclones centered in the north Pacific (Fig. 3d - f). Following the southern edge of the cyclonic wave centers, a moisture transport corridor emerges: westerly winds bring moisture to North Africa from the tropical Atlantic; southerly and southwesterly winds bring moisture from tropical Indian and Pacific Ocean towards Indian subcontinent and east Asia. Furthermore, the rotational winds of wave-1 show a clear thermal wind relationship with the pattern of surface warming. This pattern of warming can mostly be reproduced with $F_{vegice.}$

Positive δ(P-E) in both regions also results from increased tropospheric moisture content. Under PI conditions, low level winds converge towards the north Africa and subtropical east Asia, with diverging flow across the nearby ocean regions during the boreal summer (Fig. 3c). This regional circulation is a key feature of regional summer monsoon(*45*). Even without changing circulation, elevated tropospheric moisture content can result in greater moisture convergence and positive $\delta(P\text{-}E)_Q$ in subtropical Sahel and east Asia, and greater moisture divergence and negative $\delta(P\text{-}E)_Q$ in the northern and southern side of the adjacent regions. This $\delta(P\text{-}E)_Q$ pattern is a known signature of thermodynamic response to elevated CO_2, i.e., the wet-gets-wetter, dry-gets-drier paradigm(*7*, *12*, *46*). As shown in F_{vegice}, similar thermodynamic response can be induced through land cover changes besides the CO_2 change.

Discussion

Implications to hydrological cycle during Cenozoic warm intervals

The stationary wave response identified here is distinct from zonal mean Hadley circulation response or ITCZ shift. These mechanisms highlight the importance of a changing zonal mean energy budget on circulation dynamics(*14*, *30*, *47-51*). Instead, the stationary wave response in PlioMIP2 experiments is generated by spatially heterogeneous warming pattern due to perturbations to regional radiation budget induced by continental greening. This "pattern effect" may have been overlooked when examining past hydroclimate changes.

Why is F_{vegice} more effective at altering subtropical terrestrial hydroclimate compared to F_{CO2}? Land cover changes are known to be key to generating authigenic surface temperature and regional hydroclimate responses across north Africa and subtropical east Asia (*52-54*) and may even alter the strength of Atlantic meridional overturning circulation(*55*, *56*). In North Africa, expansion of desert results in enhanced surface albedo, surface cooling, and strengthened diabatic subsidence and dust emission(*57*, *58*). These responses may further suppress moist convection and perpetuate desert. Positive vegetation-precipitation feedback results in multiple equilibrium states of North African vegetation over the late Quaternary(*53*). In our simulations, atmospheric circulation responses to F_{vegice} facilitate moisture transport towards subtropical Sahel and east Asia via stationary wave response. This response is closely tied to the warming pattern generated by F_{vegice}, which does not occur in F_{CO2} (Fig. S7).

Different hydroclimate responses to F_{CO2} and F_{vegice} also reflect the difference between future and MP land surface processes. Increasing CO_2 favors reduction of soil moisture and partitioning of surface heat flux towards sensible heat, leading to enhanced surface warming. This in turn lowers relative humidity above the surface, and diminishes continental cloud cover, contributing to negative δ(P-E) on land. A similar response of surface heat flux partitioning and moisture deficit can be caused by the reduction of leaf transpiration in response to CO_2 fertilization. Both soil moisture feedback and CO_2 fertilization drive predicted future subtropical terrestrial hydroclimate change to a large extent(*15*). These changes may also contribute to muted δ(P-E) in F_{CO2} despite a modest increase in precipitation. In contrast, F_{vegice} features no physiological effect of CO_2, and produces large increases in latent over sensible heat flux across continents (Fig. S8), creating favorable conditions for a more humid troposphere. As such, moist subtropical Sahel and east Asia reflect a synergy of dynamic and thermodynamic responses to F_{vegice}. Reduced ice sheet cover, expansive northern high-latitude boreal forests, and vegetated Sahel and central Asia have been recorded during other Cenozoic warm intervals(*59-61*). These land cover changes were likely instrumental in driving changes in global mean temperature and terrestrial hydrological cycle throughout Cenozoic.

Past hydroclimate states driven by Earth System Feedbacks

Our results suggest an alternate view of the role of vegetation changes in modulating continental hydroclimate. Changes in regional circulation in the form of stationary wave responses lead to strengthened low-level winds that import moisture into the subtropical Sahel and east Asia from tropical Atlantic and Indian Ocean. This process is amplified by enhanced tropospheric moistening due to F_{vegice}, and distinct from previous mechanisms that highlight the role of the zonal mean HC and authigenic terrestrial responses to land surface changes. Simulated responses of stationary wave and tropospheric humidity clearly dominate δ(P-E) across subtropical Sahel and east Asia among models (Fig. S9). Although full feedbacks from vegetation and ice sheets are not prognostically simulated in most MP simulations (Table S1), these simulations highlight that the radiative perturbations from proxy constrained changes of vegetation and ice sheets are key to generating hydroclimate changes in the Northern subtropics. Moreover, these hydroclimate changes have minimal dependency on the prescribed MP topography and land-sea distribution (Fig. 1g).

A key implication of our findings is that MP continental hydroclimate is more appropriately viewed as part of the Earth System feedbacks instead of an immediate response to F_{CO2}. This inference is supported by the strong dependency between Gwet's AC and simulated global mean warming relative to preindustrial among models. The latter reflects model diversity in Earth System Sensitivity, given that all simulations were run with the same CO_2, and similar MP vegetation and ice sheet conditions. In contrast, intermodal spread in Gwet's AC shows little dependency on equilibrium climate sensitivity (ECS) among models (ECSs are reported in Ref(*33*)).

Moreover, the proxy data-model convergence suggests that MP terrestrial hydroclimate records do not pose a fundamental challenge to our understanding of the physics of hydroclimate change across subtropical Sahel and eastern Asia. As such, these results offer a resolution to the apparent difference between the projections of hydroclimate changes in the Sahel and subtropical east Asia in the middle-of-the-road scenarios and strong geologic evidence for moist Pliocene climate at similar levels of CO_2: while the former is dominated by short-term response to CO_2 radiative forcing and internal variability, Pliocene hydroclimate reflects long-term adjustments of the Earth system that incorporates responses from vegetation and ice sheets. Feedbacks of vegetation and ice sheets to CO_2 increase are known to amplify the response of equilibrium surface temperature to radiative forcing(*39*, *62*). We highlight that these relatively slow Earth system feedbacks are critical for understanding not only Earth's temperature responses, but also hydroclimate responses to varying CO_2. Changes in vegetation and ice sheet distributions should be carefully considered in simulating past and future climate.

Materials and Methods

Proxy-Model Comparison

Our proxy compilation builds on previous efforts to compile Pliocene hydroclimate records. These include the compilations created by Refs(*30*, *63*, *64*). The records included in these sources span a variety of proxy types, from sedimentological indicators of lacustrine environments, palynological indicators of vegetation composition, faunal remains, and stable isotope records from organic and inorganic materials. We added to these compilations by including new records of terrestrial hydroclimate dating to the Pliocene archived on the NOAA Paleoclimatology Database (https://www.ncdc.noaa.gov/data-access/paleoclimatology-data) and Pangaea Database (https://www.pangaea.de/).

To identify the average hydroclimate signal during the MP, we filtered available records based on the precision of their age models. Specifically, proxy records were required to include at least two age control points, with one age control point after the MP and a clearly identifiable age control point prior to mid-Piacenzian. For many records, this 'basal' tie point was often in the early Pliocene or Miocene. Only including records with multiple age control points reduces the likelihood that samples inferred to be from the MP actually come from earlier in the Pliocene or the early Pleistocene. For most proxy records, age control derives from a combination of magneostratigraphy (e.g. the Gauss-Matuyama boundary), radiometric dating, or biostratigraphic information. In some cases, identification of independently-dated tephra layers or correlation with the benthic oxygen isotope stack provides age control. These filtering criteria allowed us to retain a compilation of 62 records. Of the 62 records included, 30 come from paleobiological indicators like faunal remains or pollen, while the other 34 records are drawn from interpretations of sedimentary sequences or stable isotopic analyses of organic and inorganic materials (SI). A supplementary excel file with details on the proxy records, including methods, chronology, and original citation, is included with this manuscript. We note, however, that performing the analysis on the unfiltered proxy syntheses in refs. 29, 59, and 60 yield nearly identical results.

We rely on the author's original interpretation about whether the record reflects, on average, wetter or drier conditions, or no change in hydroclimate during the MP compared to late Quaternary/modern conditions. Many records are discontinuous, and cannot provide quantitative comparisons between MP climate and late Quaternary or pre-industrial conditions, and low-resolution records do not resolve climate cycles within the MP.

Our proxy data therefore represent comparisons of the change between average MP conditions and late Holocene or modern conditions. In contrast, PlioMIP2 modeling experiments are designed to target a particular orbital interval during the Pliocene (MIS KM5c), and are explicitly compared to pre-industrial control simulations(*31*). A key assumption behind our proxy model comparison is therefore that the magnitude of Pliocene hydroclimate change is greater than the impact of orbital variations. There is some evidence to support this assumption, since several high-resolution, continuous hydroclimate records suggest substantial shift in hydroclimate states from early and mid-Pliocene to early-Pleistocene. Documented hydroclimate shifts are well beyond the recorded shorter time-scale hydroclimate variability(*65-67*). However, this assumption requires further testing with additional, high resolution, well-dated hydroclimate records that can be directly compared to model outputs. Keeping in mind this source of uncertainty, our analyses focus on qualitatively assessing the agreement between proxies and models. Despite these considerations, our compilation shows similar large-scale hydroclimate features compared to previous Pliocene hydroclimate synthesis efforts, notably, wetter conditions evidenced by widespread lakes, reduced dust flux, and more mesic environments across southern and eastern Asia, north Africa, and parts of Europe. For proxy-model comparison, we include records spanning 0-67°N and 23°W-172°E. Details of broad regional trends are discussed in the SI.

Statistical Analysis

Because the majority of these records have qualitative or semi-quantitative interpretations, we assess the fit between proxies and models qualitatively. We classify modeled MP δ(P-E) as indicating wetter, drier, or no change relative to pre-industrial simulations from the same model, and we classify proxies as indicating wetter, drier, or no change based on the author's original interpretation of MP vs. present-day or late Quaternary conditions. To convert continuous, quantitative model outputs of δ(P-E) into categorical data, we classify model output as showing wetter, drier, or no change at different thresholds of % change in P-E. For instance, choosing a 10% threshold, we would classify models that show more than a 10% increase in P-E as showing wetter conditions for a particular site. We vary the threshold at 1% intervals between 1 and 100% change and separately calculate proxy-model agreement.

The degree of proxy-model agreement was assessed using Gwet's AC statistic, a metric of inter-rater agreement similar to Cohen's kappa (κ). While the latter has been used in previous proxy-model comparison studies, the nature of the Pliocene proxy data, where the vast majority of records show wetter conditions, renders Cohen's κ statistic less robust(*68*). Cohen's κ is known to perform poorly as a result of `Cohen's paradox' whereby the statistic underestimates the true agreement between raters in cases of skewed distributions of ratings across categories(*68*). We therefore use a related metric known as Gwet's AC, which is known to be resistant to this paradox. The Gwet's AC statistic is similar to Cohen's in that the AC statistic is:

$$AC = \frac{P_a - P_{exp}}{100\% - P_{exp}}$$

Where P_a is the actual percentage of agreement between proxies and models (e.g. the percentage of wetter sites that are correctly classified by the model as wetter, the percentage of drier sites correctly classified by the model, etc.), and P_{exp} reflects the expected percentage of agreement between raters (e.g. proxies and models) by chance alone. The Gwet's AC statistic is identical to Cohen's κ but uses a different formulation for P_{exp} that is not susceptible to Cohen's paradox. Statistical significance of the Gwet's AC statistic was calculated according to the error estimator and methods outlined in ref(*68*). Results of statistical significance testing are presented in Figure S3.

To avoid weighting our analysis towards regions with a greater density of proxy records, records less than 150 km that featured the same sign of change (e.g. both showing wetter, drier or no change) from each other were combined into one site. However, in cases with records showing opposite signs of change, we retain both records since in many cases there is not enough information to determine which record is more reliable, and excluding both would decrease the data coverage of our proxy compilation in key regions like East Asia (Figure S2).

In the absence of *a priori* evidence that proxies reflect hydroclimate in a particular season, patterns of proxy-model agreement are assessed using annually averaged P-E. We independently assess the fit between proxies and models for winter (December - February) and summer (July-September) separately (Figure S4). The fit is much higher across all models and the multi-model mean for July-September rainfall. Proxy-model agreement for winter rainfall alone show very low values of Gwet's AC statistic, suggesting that winter rainfall changes do not explain a significant component of the pattern seen in proxy record. Furthermore, intermodel spread in Gwet's AC values on annually averaged rainfall show a strong correlation with intermodal Gwet's AC results calculated for July-September P-E (Fig. 2) at nearly all threshold values of P-E. This suggests that the summer seasonal signal, which is also the largest signal across model simulations (Fig. 1), drives the overall pattern of proxy-model agreement across models.

PlioMIP2 Ensemble

We use a suite of model simulations conducted as part of the 2nd Pliocene Model Intercomparison Project (PlioMIP2) (*35*, *69*-*75*). Boundary conditions are derived from the PRISM4 dataset(*32*). PRISM4 boundary conditions include information on land distributions, topography and bathymetry, vegetation, soils, lakes, and land ice cover. Two experimental protocols were developed, one implementing Pliocene conditions with a modern land/sea mask, and the enhanced experiment that included all boundary conditions(*31*, *76*). pCO$_2$ is prescribed at 400 ppm. Other trace gases, orbital parameters, and solar output were set to be identical to the pre-industrial control simulation of each model.

Modeling groups were given the option to either prescribe vegetation changes or simulate vegetation changes using a dynamic global vegetation model. For the latter experiment, model simulations were started with pre-industrial vegetation and the model was allowed to spin up until a new equilibrium distribution of vegetation was achieved. We provide basic information on configuration of each of the PlioMIP2 models used in our analyses in Table S1, and is provided in the previous study(*33*). We note that only one modeling group in the suite of simulations we analyzed opted to use a dynamic configuration for vegetation, suggesting that the choice of dynamic vs. static vegetation is not the primary source of spread across model results. We also note that models show varying levels of agreement with the signal in proxies (Fig. 2), suggesting that our results are not trivial (e.g. models with prescribed vegetation reproduce said vegetation) since the spatial pattern of hydroclimate in each model appear to depend on model design.

Sensitivity experiments using Community Earth System Model version 2 (CESM2)

Despite the overall similarity in geography and topography to present-day, MP boundary conditions feature several changes in ocean gateways, islands, and lake distributions that may influence regional climate(*32*, *37*, *77*-*79*). PlioMIP2 simulations also feature expanded grassland replacing the subtropical desert of North Africa and central Asia and afforestation at northern high latitudes as well as deglaciated western Antarctic and most of the Greenland(*32*).

To isolate the mechanisms responsible for Pliocene hydroclimate changes, we carried out two new experiments with CESM2 that decompose simulated responses to the full MP climate forcing (F_{all}) into responses to forcings from elevated CO$_2$ (F_{CO2}), changes in paleo-geography and -topography (F_{geotop}), and changes in biome distribution and ice sheets (F_{vegice}). These new experiments separately feature 1) a 400 ppm CO$_2$ and preindustrial boundary conditions (E400); 2) preindustrial vegetation and ice sheets, but otherwise MP CO$_2$ and boundary conditions (Eo400). The design and naming convention of these simulations follow the Tier II PlioMIP2 protocol(*31*). All simulations are run with 0.9x1.6° resolution for atmosphere and land, and 1° nominal resolution for ocean and ice component, resulting in ~100 km resolution of all model components.

These new simulations are carried out for over 300 model years. Diagnostics of equilibrium by global mean top of the atmosphere radiation imbalance and surface temperature are shown in Fig. S10. To produce climatology, we average the last 100 years of the model simulation. Eo400 and E400 together with the published full forcing (Eoi400) and preindustrial experiments (E280) allow the decomposition of climate responses (denoted as R) to F_{all} into the sum of responses to individual forcings: R(F_{all}) = R(F_{vegice}) + R(F_{geotop})+R($_{CO2}$), for which R(F_{all}) = R(Eoi400) – R(E280); R(F_{geotop}) = R(Eo400) – R(E400); R(F_{vegice}) = R(Eoi400) – R(Eo400); R(F_{CO2})=R(E400) – R(E280).

Development of moisture budget analysis

To diagnose the causes of δ(P-E) in model simulations, we further developed and applied the moisture budget analysis(*41*) to the multimodel mean of the PlioMIP2 simulations. With only monthly data available, our derivation aims to facilitate the comparison of a pair of experiments and the evaluation of existing hypotheses regarding the cause of MP hydroclimate change (e.g. identifying whether MP hydroclimate anomalies results from zonal mean changes or stationary wave changes).

Following equation (13) in Ref(*41*) on pressure coordinates, precipitation minus evaporation is balanced by changes in the moisture tendency and moisture convergence :

$$P - E = -\frac{1}{g\rho_w}\frac{\partial}{\partial t}\int_0^{P_s} qdp - \frac{1}{g\rho_w}\nabla\cdot\int_0^{P_s} uqdp \qquad (1)$$

In Equation (1), g is geopotential acceleration, ρ_w is the density of water, P_s is surface pressure, and q isspecific humidity, p: pressure. For a pair of experiments, experiment 1 is the control case (e.g. preindustrial) and experiment 2 is the sensitivity experiment (e.g. Pliocene), the small perturbation method tells us that $q_2 = q_1 + \delta q;\ u_2 = u_1 + \delta u;\ (P-E)_2 = (P-E)_1 + \delta(P-E); and\ P_{s2} = P_{s1} + \delta P_s$. We can therefore decompose the perturbations to P-E into contributions from the anomalous moisture tendency, changes in convergence due to changes in wind, moisture, and the interaction of these changes, as well as a residual term:

$$\delta(P-E) = -\frac{1}{g\rho_w}\frac{\partial}{\partial t}\int_0^{P_{s2}} \delta q dp - \frac{1}{g\rho_w}\nabla\cdot\int_0^{P_{s2}}(q_1\delta u + u_1\delta q + \delta u\delta q)dp + resi \quad (2)$$

$$resi = -\frac{1}{g\rho_w}\frac{\partial}{\partial t}q_1\delta P_s - \frac{1}{g\rho_w}\nabla\cdot(u_1 q_1 \delta P_s) \quad (3)$$

Applying Reynold's decomposition, we can separate the total change in a given quantity into its temporal mean (e.g. monthly or annual climatology), denoted via an overbar, and higher frequency temporal fluctuations, denoted via a prime. Such that:

$$\delta q = \delta\bar{q} + \delta q', \delta u = \delta\bar{u} + \delta u' \quad (4)$$

$$\delta(P-E) = \overline{\delta(P-E)} + \delta(P-E)', u_1 = \bar{u}_1 + u_1', q_1 = \bar{q}_1 + q_1', P_{s2} = \bar{P}_{s2} + P_s' \quad (5)$$

Given that we are interested in understanding the contributions from zonal mean circulation changes compared to other changes, we further separate $\delta\bar{u}$ into changes in zonal mean, indicated by square brackets ([]) and changes in deviations from the zonal mean (i.e., the stationary wave), which is indicated by an asterisk (*):

$$\delta\bar{u} = [\delta\bar{u}] + \delta\bar{u}^*$$

Using these expansions, we can rephrase the anomalous moisture budget in equation (2) to separate out the contributions due to zonal mean and stationary wave. The updated form of equation 2 is:

$$\overline{\delta(P-E)} = -\frac{1}{g\rho_w}\frac{\partial}{\partial t}\int_0^{\overline{P_{s2}}} \overline{\delta q}dp - \frac{1}{g\rho_w}\nabla\cdot\int_0^{\overline{P_{s2}}}\left(\bar{u}_1\overline{\delta q} + \bar{q}_1([\delta\bar{u}] + \delta\bar{u}^*) + \delta\bar{u}\delta\bar{q}\right)dp + resi\ 1 + resi\ 2$$

(6)

Residual term 1 quantifies the effects of topographic changes (δP_s). Residual term 2 (resi 2) quantifies combined effects of transient eddies moisture transport and influxes:

$$resi\ 1 = -\frac{1}{g\rho_w}\frac{\partial}{\partial t}(\overline{q_1'\delta P_s'} + \overline{q_1\delta P_s}) + -\frac{1}{g\rho_w}\nabla\cdot\overline{(\overline{u_1} + u_1')(\overline{q_1} + q_1')(\delta\overline{P_s} + \delta P_s')}$$

$$resi\ 2 = -\frac{1}{g\rho_w}\frac{\partial}{\partial t}\overline{\delta q' P_s'} + \frac{1}{g\rho_w}\nabla\cdot\left[\overline{(\bar{u}_1\delta q' + u_1'\delta\bar{q} + q_1'\delta\bar{u} + \bar{q}_1\delta u' + \delta u'\delta\bar{q} + \delta\bar{u}\delta q')P_s'}\right] - \frac{1}{g\rho_w}\nabla \cdot\int_0^{\overline{P_{s2}}}\overline{(\delta q'\delta u' + q_1'\delta u' + u_1'\delta q')}dp$$

Calculating residual terms 1 and 2 require high frequency outputs of surface pressure, three-dimensional specific humidity and horizontal winds, which are not available in PlioMIP2 database. Also, even at 6-hourly resolution, the calculated eddy terms are insufficient to close the moisture budget with reanalysis observational data(*41*). Thereby, resi 1 and resi 2 are not explicitly calculated in our calculations and quantified as a combined residual (i.e., the difference between P-E changes and the sum of other terms in the moisture budget equation).

Monthly climatologies of surface pressure, precipitation, evaporation, and three-dimensional horizontal winds, and specific humidity are used to calculate the remaining terms in equation 6. From the left to right, the first term in equation 6 ($-\frac{1}{g\rho_w}\frac{\partial}{\partial t}\int_0^{\overline{P_{s2}}}\overline{\delta q}dp$) is the moisture tendency term, which quantifies contributions to $\overline{\delta(P-E)}$ from changes in seasonal cycle. The term $-\frac{1}{g\rho_w}\nabla\cdot\int_0^{\overline{P_{s2}}}\left(\bar{u}_1\overline{\delta q}\right)dp$ describes contributions from changes in climatological mean tropospheric moisture content; $-\frac{1}{g\rho_w}\nabla\cdot\int_0^{\overline{P_{s2}}}(\bar{q}_1[\delta\bar{u}])dp$describes contributions from changes in zonal mean circulation; $-\frac{1}{g\rho_w}\nabla\cdot\int_0^{\overline{P_{s2}}}(\bar{q}_1\delta\bar{u}^*)dp$ describes contributions from changes in stationary wave kinetics. Finally,$-\frac{1}{g\rho_w}\nabla\cdot\int_0^{\overline{P_{s2}}}(\delta\bar{u}\delta\bar{q})dp$ describes contributions from covarying changes in mean moisture content and horizontal circulation.

Acknowledgments

The authors would like to thank all the modelling groups who provided the PMIP3 and PMIP4 outputs for this analysis, WCRP, CMIP panel, PCMDI, ESGF infrastructures for sharing data, WCRP and CLIVAR for supporting the PMIP project. We would also like to thank H. Dowsett for developing PRISM4D datasets.

Computing: The CESM2 simulations are performed with high-performance computing support from Cheyenne (doi:10.5065/D6RX99HX) provided by NCAR's Computational and Information Systems Laboratory, sponsored by the National Science Foundation.

The IPSL-CM6A-LR simulation was run on the Très Grande Infrastructure de Calcul (TGCC) at Commissariat à l'Energie Atomique (gencmip6 project) under the allocations 2016-A0030107732, 2017-R0040110492 and 2018-R0040110492 (project gencmip6) provided by GENCI (Grand Equipement National de Calcul Intensif).

The model simulations with EC-Earth3 and the data analysis were performed using resources provided by ECMWF's computing and the Swedish National Infrastructure for Computing (SNIC) at the National Supercomputer Centre (NSC), which is partially funded by the Swedish Research Council through grant agreement no. 2018-05973.

AAO and WLC acknowledge JAMSTEC for use of the Earth Simulator supercomputer.

Funding:

U.S. National Science Foundation grant 1814029 (R. Feng)

U.S. National Science Foundation grant 1903650 (R. Feng)

U.S. National Science Foundation grant 1903148 (T. Bhattacharya)

France ANR HADoC (ANR-17-CE31-0010) (C. Contoux).

Swedish Research Council (Vetenskapsrådet; grant nos. 2013-06476 and 2017-04232) (Q. Zhang)

Japanese JSPS Kakenhi grant 17H06104 and MEXT Kakenhi grant 17H06323 (W. Chan and A. O)

The PRISM4 reconstruction and boundary conditions used in PlioMIP2 were funded by the U.S. Geological Survey Climate and Land Use Change Research and Development Program. Any use of trade, firm, or product names is for descriptive purposes only and does not imply endorsement by the U.S. Government.

Author contributions: Conceptualization: RF, TB, BOB, AMH
Methodology: RF, TB, MC
Investigation: RF, TB
Visualization: RF, TB
Writing—original draft: RF, TB
Writing—review & editing: all authors

Competing interests: none.

Data availability: PlioMIP2 simulations that are part of the Climate Model Intercomparison Project 6 (CMIP6) can be found via Earth System Grid Federation:
EC-Earth3: https://doi.org/10.22033/ESGF/CMIP6.4804
IPSL-CM6A-LR: https://doi.org/10.22033/ESGF/CMIP6.5230
GISS-E2-1-G: https://doi.org/10.22033/ESGF/CMIP6.7227
CESM2: https://doi.org/10.22033/ESGF/CMIP6.7675
HadGEM3: https://doi.org/10.22033/ESGF/CMIP6.12130IPSL-CM6A-LR:

The sensitivity simulations with CESM2 are available on Cheyenne supercomputer (will be transferred to a public database upon publication of this manuscript). The current path is /glade/p/cgd/ccr/people/ranfeng/pliomip2.

Code availability:
The standard model code of the COSMOS version COSMOS-landveg r2413 (2009) is available upon request from the Max Planck Institute for Meteorology in Hamburg (https://www.mpimet.mpg.de).
Source code of CESM2 can be downloaded from https://escomp.github.io/CESM/versions/cesm2.1/html/downloading_cesm.html.
Moisture budget analysis code can be found at Cheyenne supercomputer with the path /glade/p/cgd/ccr/people/ranfeng/pliomip2/ensemble/budget/pe_budget_season.ncl
PRISM4 boundary condition data sets can be found here: https://geology.er.usgs.gov/egpsc/prism/7.2_pliomip2_data.html

Figures and Tables

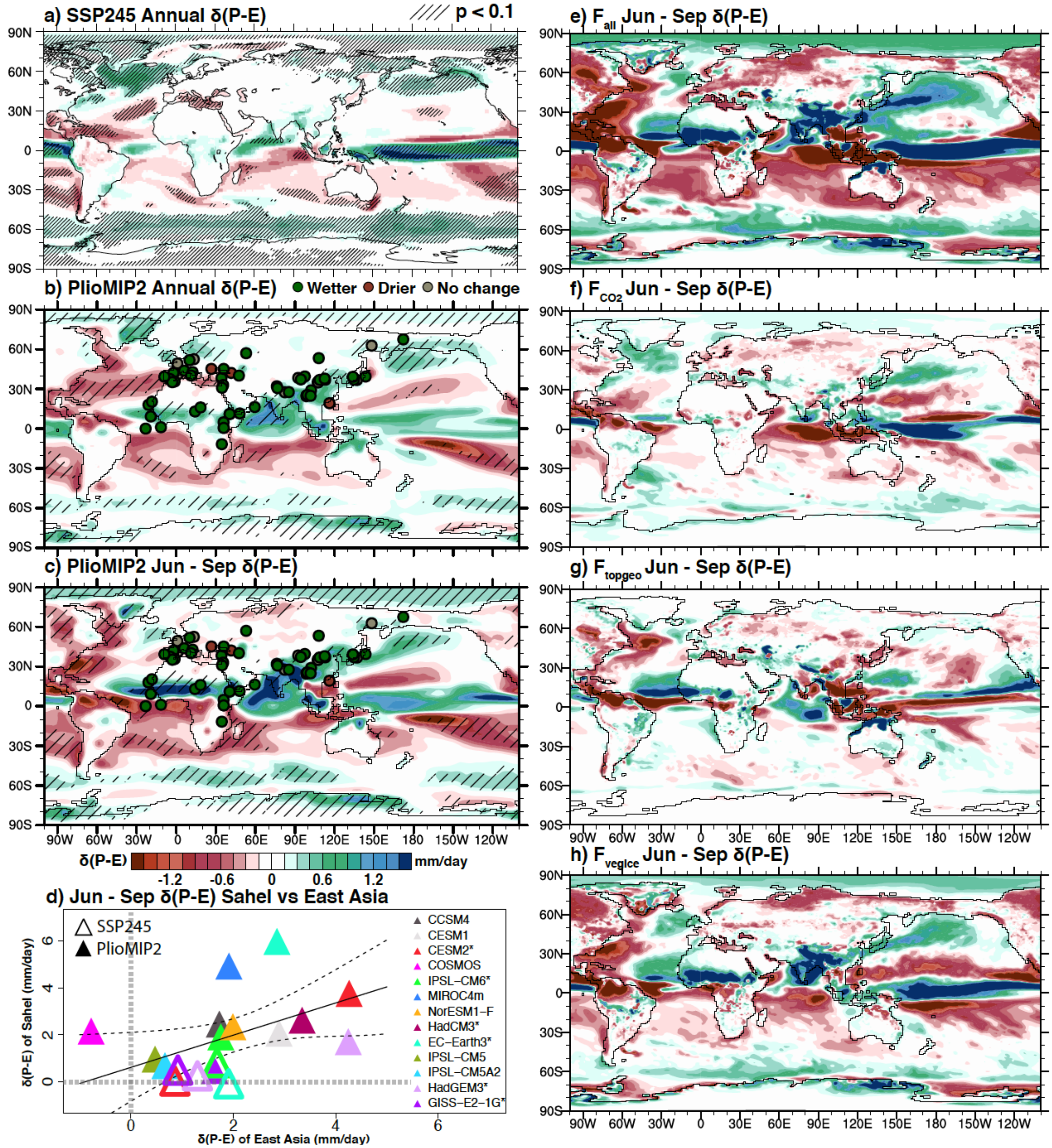

Fig. 1. δ(P-E) in Pliocene proxy records and both future and Pliocene simulations. (a) δ(P-E) measured by the difference between 2081 to 2100 and 1986 to 2005 following Shared Socioeconomical Pathway 245. (b) – (c) Pliocene proxy, annual and boreal summer (June to September) mean δ(P-E) of PlioMIP2 ensemble. d) Correspondence between subtropical Sahel (10° - 20°N, 10°W – 25°E) and east Asia (20° - 30°N, 80°E – 100°E) δ(P-E) simulated by PlioMIP2 experiments and a subset of SSP245 experiments with the same models (model names are marked with asterisks). (e) to (h) δ(P-E) in response to full Pliocene climate forcing conditions (F_{all}), CO_2 forcing alone (F_{CO2}), changes in topography and geography ($F_{topogeo}$), and changes in vegetation and icesheet (F_{vegice}) simulated by Community Earth System Model version 2. SSP245 ensemble includes BCC-CSM2-MR, CESM2, CESM2-WACCM, CanESM5, CNRM-CM6-1, CNRM-ESM2-1, EC-

Earth3.3, GISS-E2-1-G, HadGEM3-GC31-LL, IPSL-CM6A-LR, MIROC6, MIROC-ES2L, MRI-ESM2-0, NESM3, UKESM1-0-LL. In (b) to (h), δ(P-E) is the difference between Pliocene and preindustrial simulation. Area significant against multi-model spread is hatched in (a) to (c) identified by Welch's t-test (p<0.1).

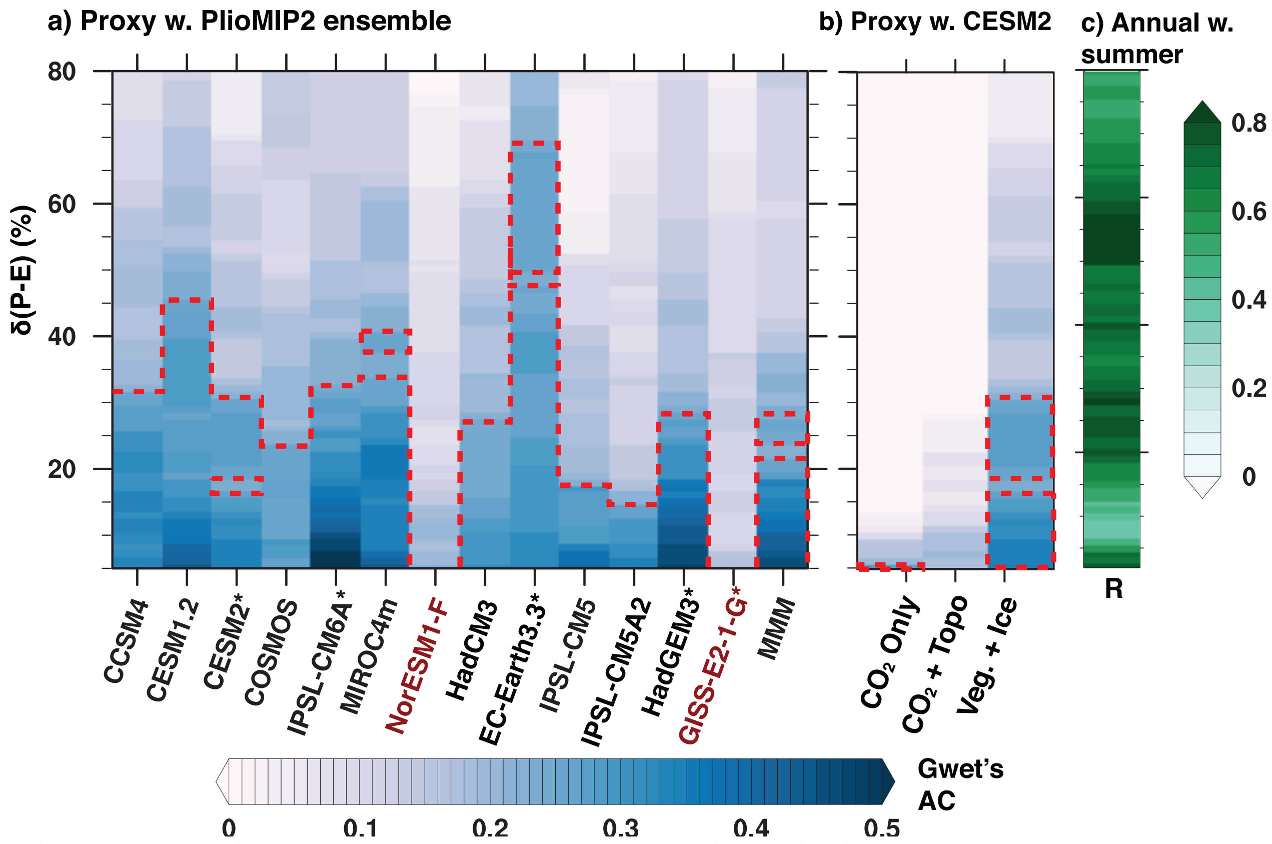

Fig. 2. Degree of agreement between proxy hydroclimate indicators and simulated δ(P-E), and correlation between annual mean and boreal summer signal. Proxy-model fit is assessed using a measure of categorical agreement between two datasets called Gwet's AC. For a given % threshold change in P-E in models, higher (lower) values indicate that proxies and models agree (disagree) that a given location is wet, dry, or neutral. Area within dashed line indicates statistically significant agreements. a) Gwet's AC agreement between individual models, MMM, and proxies at different thresholds. CMIP6 models are identified with an asterisk. b) Agreement between proxies and δ(P-E) due to F_{CO2}, combined F_{CO2} and F_{geotop}, and F_{vegice} simulated by CESM2. c) Linear correlation (e.g. r value) between annual mean and boreal summer averages across individual models of PlioMIP2 ensemble. CMIP6 models are identified with an asterisk.

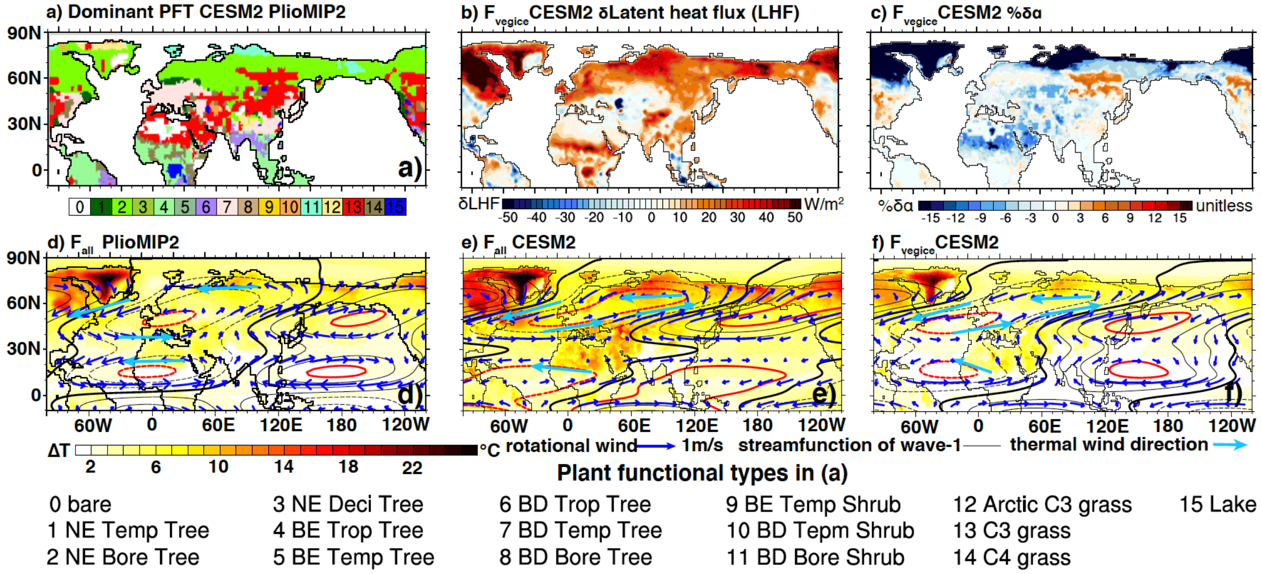

Fig. 3. Pliocene vegetation and ice sheet distribution, and responses of boreal summer surface radiation, temperature, and stationary wave to F_{all} and F_{vegice}. (a) vegetation and ice sheet distribution: the plant functional type (PFT) with the highest percentage in a grid cell is shown. (b) Surface latent heat flux and (c) albedo changes induced by F_{vegice}. (d) – (f) changes of surface temperature (color shaded), and 600 hPa wave-number 1 (contour) and rotational winds (vectors) of stationary wave in response to F_{all} simulated by PlioMIP2 ensemble and CESM2, and to F_{vegice} simulated by CESM2.

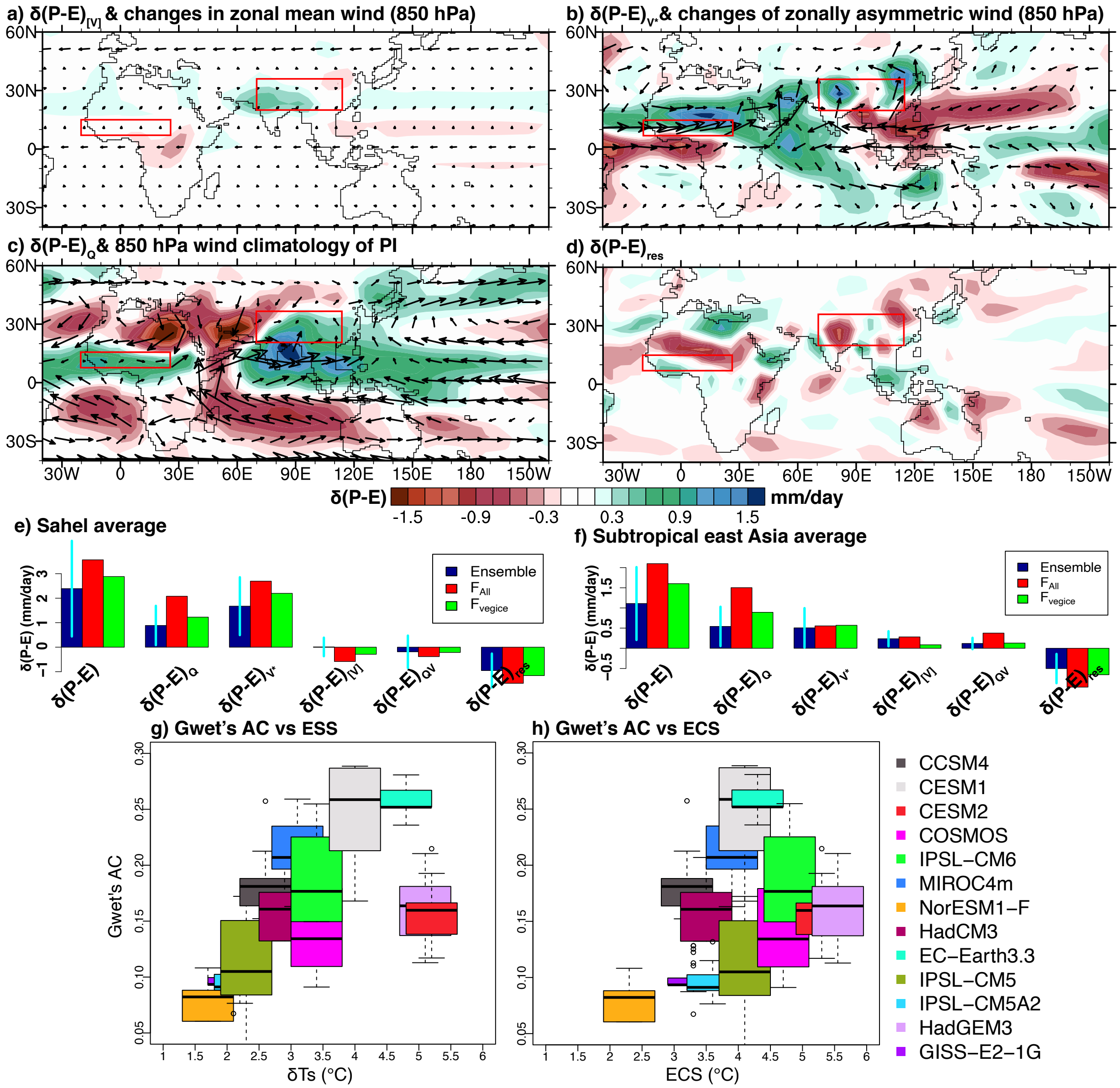

Fig. 4. Moisture budget decomposition of boreal summer δ(P-E) and the potential linkage of δ(P-E) with Earth System Sensitivity (ESS) and Equilibrium Climate Sensitivity (ECS). (a) to (d) contributions to δ(P-E) from tropospheric moistening (δ(P-E)$_{Q}$), changes of stationary wave dynamics (δ(P-E)$_{V*}$), zonal mean circulation(δ(P-E)$_{[V]}$), and nonlinear effects of tropospheric moistening and changing circulation (δ(P-E)$_{QV}$) as well as a residual term(δ(P-E)$_{RES}$). (e) and (f) Regional mean (red boxes in (a) to (d)) moisture budget for subtropical Sahel and East Asia simulated by PlioMIP2 ensemble, and CESM2 with F$_{all}$ and F$_{vegice}$. Error bars show 1 standard deviations of model spread. g) to h) Gwet's ACs of individual PlioMIP2 simulations as a function of global mean warming (δTs, which quantifies ESSs), and ECSs of these models. δTs and ECSs are from Ref(*33*). Boxplots show the spread of Gwet's AC from using 20% to 60% of δ(P-E) as thresholds (Method).

advances.sciencemag.org/cgi/content/full/sciadv.[abj2939]/DC1

Supplementary Materials for

Past terrestrial hydroclimate driven by Earth System Feedbacks

R. Feng[1*], T. Bhattacharya[2], B. Otto-Bliesner[3], E. Brady[3], A. Haywood[4], J. Tindall[4], S. Hunter[4], A. Abe- Ouchi[5], W. -L. Chan[5], M. Kageyama[6], C. Contoux[6], C. Guo[7], X. Li[8], G. Lohmann[9], C. Stepanek[9], N. Tan[10], Q. Zhang[11], Z. Zhang[8], Z. Han[12], J. R. Williams[13], D. J. Lunt[13], H. Dowsett[14]

*Corresponding author. Email: ran.feng@uconn.edu

This PDF file includes:

- Supplementary Text
- Table S1
- Figs. S1 to S8
- References (80 to 113) (if applicable—these should refer only to references in the SM)

Other Supplementary Materials for this manuscript include the following:

- Data S1

Supplementary Text

Sensitivity experiments using CESM2

We carried out two new simulations using the community Earth System Model version 2 (individual model components are Community Atmospheric Model version 6, Community Land Model version 5, Parallel Ocean Program version 2, and Community Ice CodE version 5) to quantify individual effects of elevated CO_2, changes in paleo-geography and topography, and vegetation and ice sheets on mid-Pliocene P-E changes. These new experiments separately feature Pliocene levels of carbon dioxide (400 ppm CO_2) coupled with preindustrial boundary conditions (e.g. ice sheets and vegetation and geography and topography) in the case of E400. This simulation was used to isolate the influence of Pliocene CO_2 (F_{CO2}). For Eo400, the simulation features preindustrial vegetation and ice sheets and otherwise mid-Pliocene CO_2 and boundary conditions, and can be compared to the full Pliocene simulation to isolate the influence of vegetation and ice cover (F_{vegice}). The influence of geography and topography (F_{geotop}) was isolated by subtracting E400 from Eo400.

Eo400 and E400 are initialized with ocean states and terrestrial carbon and nitrogen states from previously published runs of the mid-Pliocene, and preindustrial which feature the same geography and topography as Eo400 and E400 respectively. Each of which was run for more than 500 model years. Model equilibrium is diagnosed with global mean net top of atmosphere radiation imbalance (F_{net}) and global mean surface temperature (T_s). For the last 100 model years, global mean F_{net} of all simulations is ~ 0.2W/m^2 for both simulations, and trends of global mean T_s are 0.1 and 0.2°C per century (Fig. S9).

Proxy recorded Pliocene regional hydroclimate patterns

We compiled Pliocene hydroclimate indicators from published records (Table S1). We rely on the author's original interpretations about whether the record reflects, on average, wetter or drier conditions, or no change in hydroclimate during the MP compared to late Quaternary/modern conditions. Below, we provide a review of published studies on broad regional trends evident in the proxy records.

Europe and the Mediterranean: Evidence of wetter MP conditions in Europe and the Mediterranean primarily come from sedimentological evidence of expanded lacustrine environments and palynological indicators of more mesic vegetation. For instance, pollen and macrobotanical remains from the lagerstatte deposit at Willershausen in modern Germany provide evidence of a slightly wetter climate(*64*) and pollen records(*80*) document mesic vegetation across the Iberian Peninsula and north Africa. Evidence from the Dacian Basin records an interval of high salinity at 3 Ma towards the end of the MP, which could reflect changes to the regional water budget, but has been interpreted to reflect higher water levels in the Black Sea that slightly postdate the MP(*81*). This coheres with the interpretations of(*82*), which suggest a decrease in winter precipitation in midlatitude Europe between 4 and 3 Ma.

Africa and the Middle East: Continuous Plio-Pleistocene records of dust flux from off the coast of west Africa have been interpreted as evidence of long-term drying(*83*, *84*). Several records also provide evidence of the expansion of ecosystems dominated by C4 plant species(*65*, *85*-*87*). Like pollen records, the interpretation of these records is complex since these ecosystem shifts may reflect hydroclimate, but these may also be driven by changes in pCO$_2$ or fire regimes. However, records of stable isotopes of oxygen and hydrogen in organic and inorganic materials, which have been interpreted as reflecting an 'amount effect,' whereby higher rainfall rates result in a more depleted isotopic signature, reflect a wetter MP(*85*, *88*, *89*). Pollen data , dust flux records, and sedimentological indicators also show wetter conditions in the Levant and Arabian Peninsula during the MP(*90*, *91*). This is corroborated by a recently published stable isotopic record of hydroclimate from a cave in the Negev Desert(*92*).

South and East Asia: Evidence of wetter MP conditions in South and East Asia are primarily drawn from palynological transfer functions or faunal remains(*3*, *93*, *94*). However, in many regions these inferences are corroborated by other indicators(*95*). In the Qaidam Basin (northeastern Tibetan plateau), and in southwest China's Yuanmou region, sedimentological indicators provide evidence of a wetter MP in regions where pollen evidence suggests little change(*91*, *96*-*99*). In the Loess Plateau region, multiple proxies provide evidence of no change or drier conditions at the MP compared to the Pleistocene(*100*, *101*). However, evidence from mapping the total extent of loess deposits at different intervals during the Neogene and Quaternary provides evidence of a more mesic climate during the MP(*102*).

	Modeling Group	Model reference	Vegetation
CCSM4	National Center for Atmospheric Research	(*103*)	Prescribed according to PRISM4(*32*)
CESM1.2	National Center for Atmospheric Research	(*104*)	Prescribed according to PRISM4(*32*)
CESM2	National Center for Atmospheric Research	(*34*)	Prescribed according to PRISM4(*32*)
COSMOS	Alfred Wegener Institute, Germany	(*105*)	Dynamic
EC-Earth 3.3	Stockholm University, Sweden	(*106*)	Prescribed according to PRISM4(*32*)
HadCM3	University of Leeds, UK	(*107*)	Prescribed according to PRISM4(*32*)
IPSL-CM5	Laboratoire des Sciences du Climat et de l'Environnement (LSCE), France	(*108*)	Prescribed according to PRISM4(*32*)
IPSL-CM5A2	Laboratoire des Sciences du Climat et de l'Environnement (LSCE), France	(*108*)	Prescribed according to PRISM4(*32*)
IPSL-CM6	Laboratoire des Sciences du Climat et de l'Environnement (LSCE), France	(*109*)	Prescribed according to PRISM4(*32*)
MIROC4m	Center for Climate System Research (Uni. Tokyo), JAMSTEC	(*110*)	Prescribed according to PRISM4(*32*)
NorESM-1L	Norwegian Research Centre, Bjerknes Centre	(*111*)	Prescribed according to PRISM4(*32*)
HadGEM3	UK Met Office	(*112*)	Prescribed according to PRISM4(*32*)
GISS-E2-1G	NASA Goddard Institute for Space Studies	(*113*)	Prescribed according to PRISM4(*32*)

Table S1

Models from PlioMIP2 archive used in our analyses. The last 100 years of each model simulation are averaged together to calculate the ensemble mean. Most simulations except COSMOS used the prescribed vegetation. COSMOS used dynamic vegetation model.

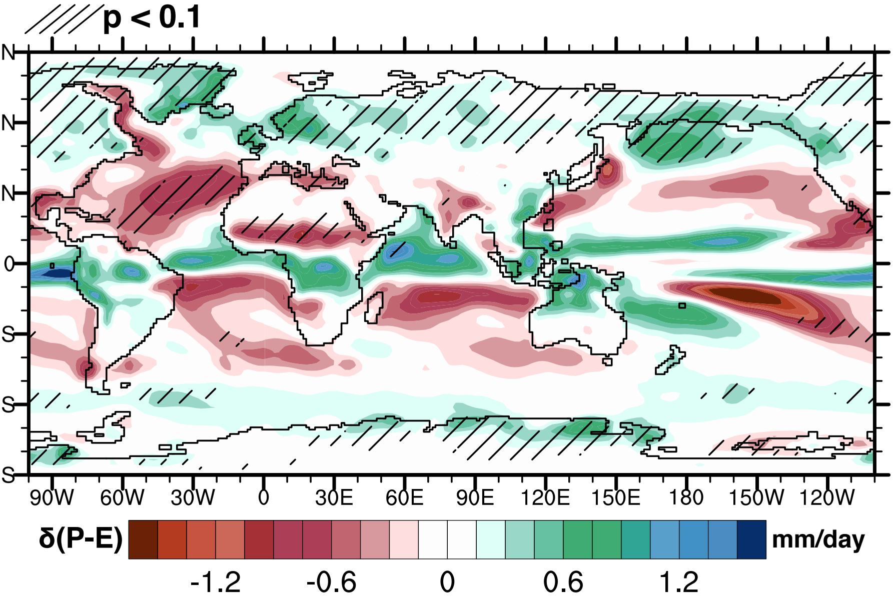

Fig. S1.

Simulated terrestrial hydroclimate change between PlioMIP2 simulations and PI (δ(P-E)) during the boreal winter (December to March).

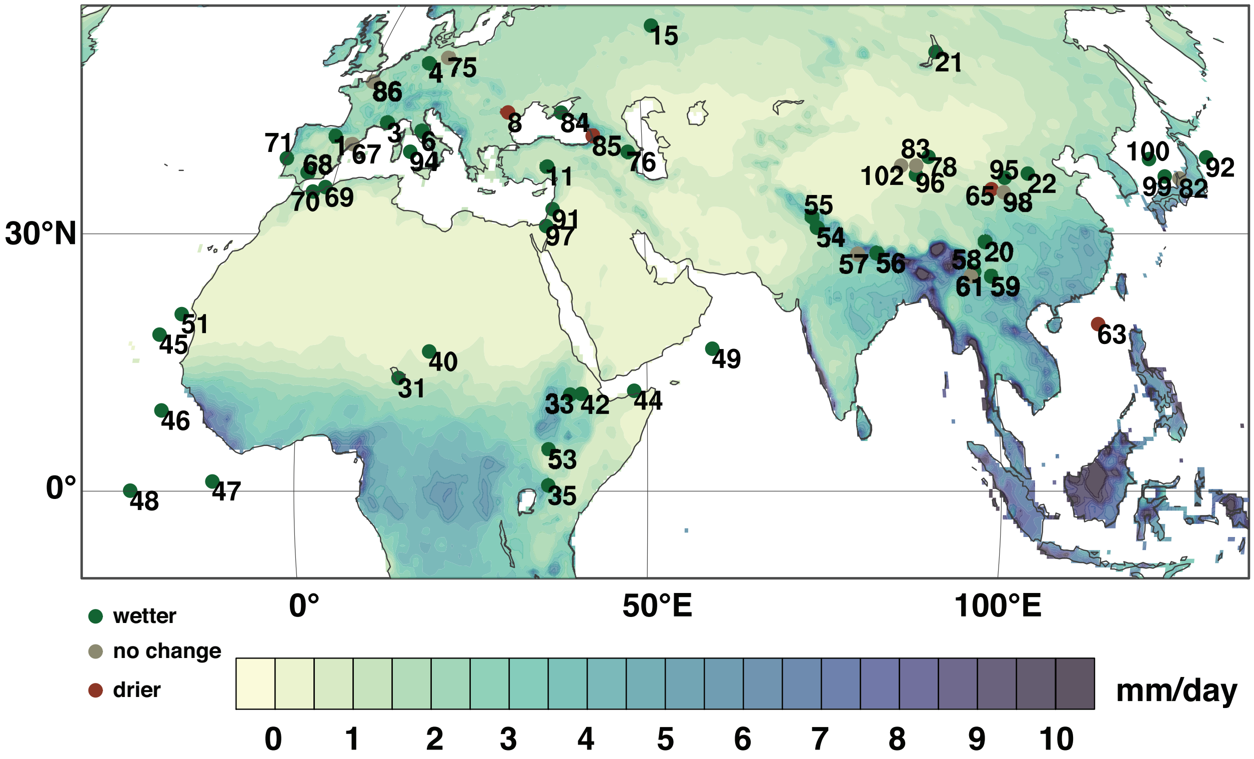

Fig. S2.

Locations of sites used in our proxy compilation, set against a background of annual average rainfall rate from the GPCC. Co-located sites were combined if they were less than 150 km apart and featured same-signed anomalies. These include: Site 35, 72; 77, 22; 79,61; 65, 66; and 61,79,58,191. Site numbers correspond to site indices in supplemental file (SI_pliocene_hydroclimate.xlsx), which also contains information on proxies, chronology, and references. Note that numbers are non-continuous, since some sites in our original compilation were excluded by our quality control standards for proxy data. Original references for each site are included in the main text Methods section.

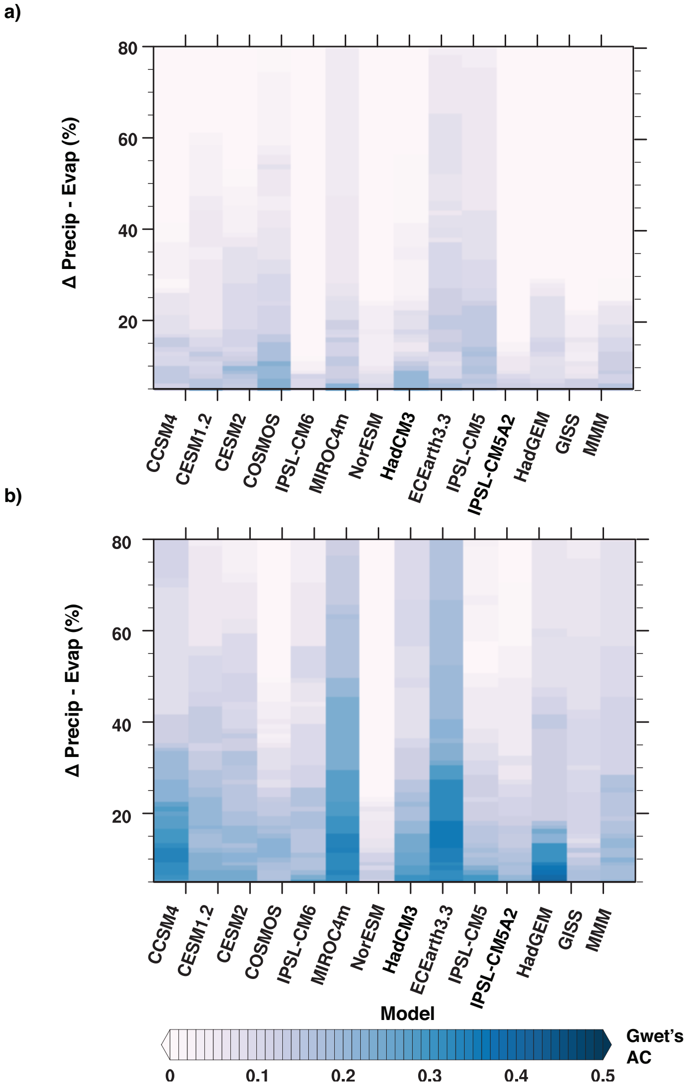

Fig. S3

Agreement between proxies and models, including the multi-model mean (MMM), in different seasons. (a) shows Gwet's AC value at different thresholds of % change in P-E for winter (December-March) rainfall only, and b) shows Gwet's AC values for summer rainfall only (July-September).

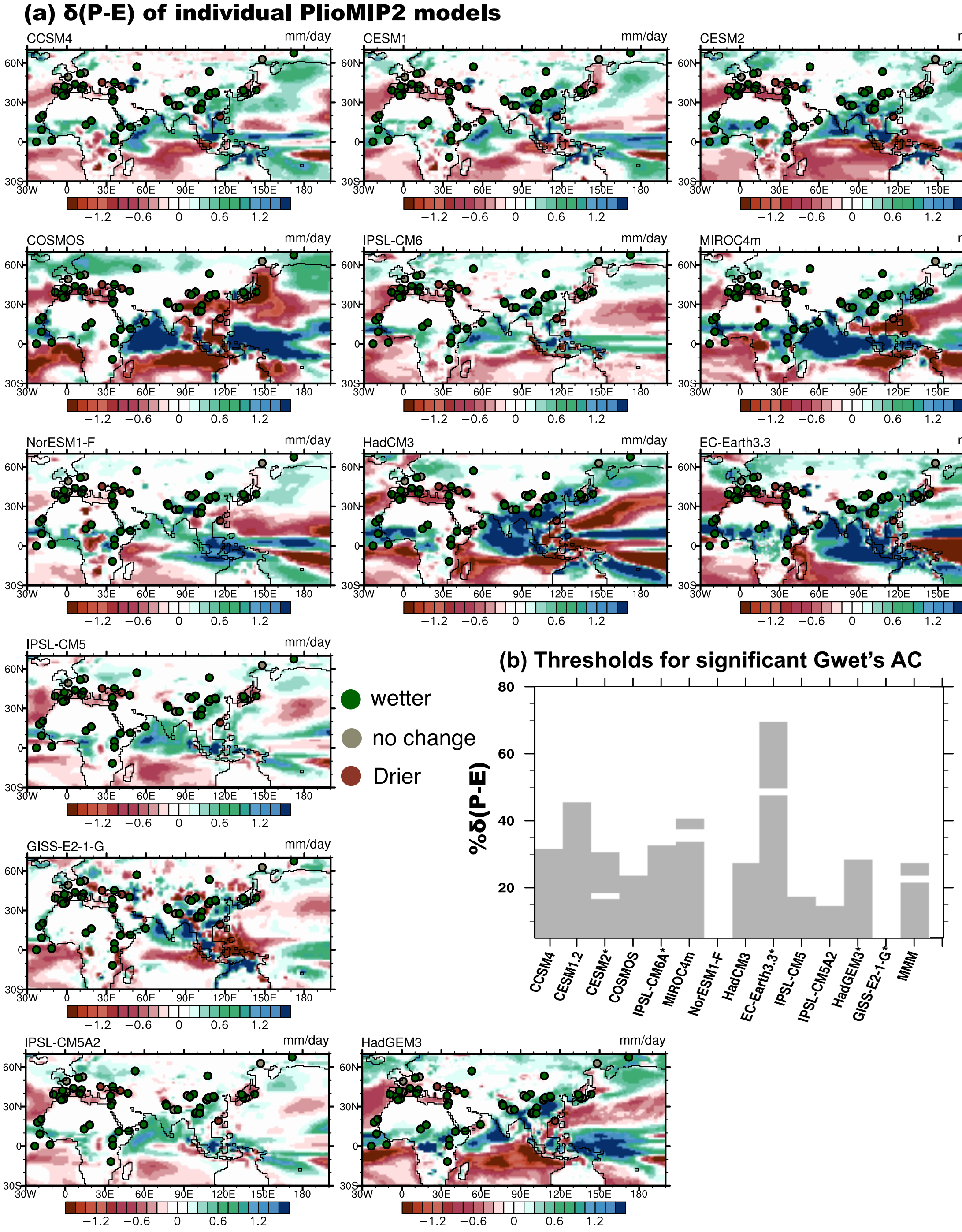

Fig. S4.

(a) Change in annual mean precipitation minus evaporation (δ(P-E)) in individual PlioMIP2 models relative to preindustrial. Model name is given in the in top left of each panel, and proxy records are overlaid to show whether a given record shows wetter, drier, or no change. (b) Range of significance thresholds of %δ(P-E) at which the agreement between proxies and models shown in Figure 2 in the main text is significant, with gray colors indicating significant values of Gwet's AC at that percentage threshold.

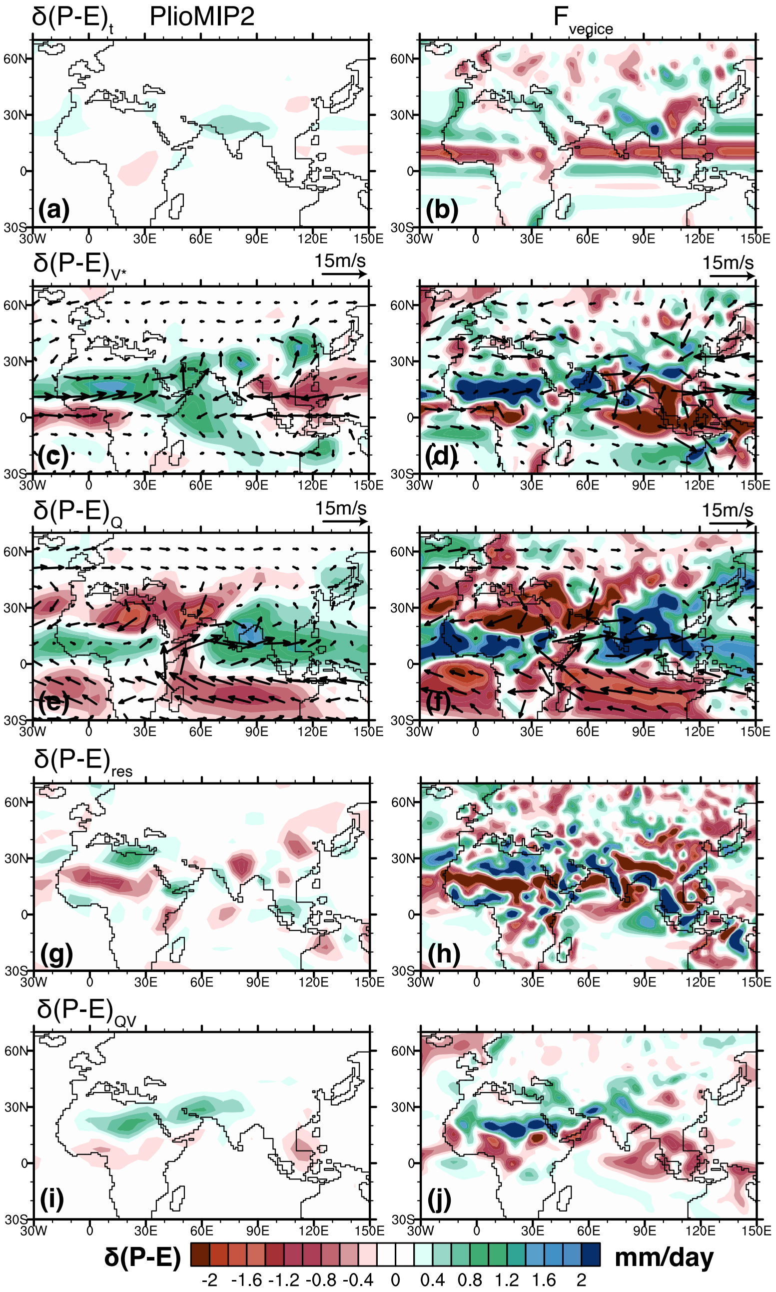

Fig. S5

June to September contributions to δ(P-E) from (a) and (b) change in the seasonal cycle ($\delta(P\text{-}E)_t$), (c) and (d) stationary wave dynamics ($\delta(P\text{-}E)_{V*}$), e) and f) tropospheric moistening ($\delta(P\text{-}E)_Q$), (g) and (h) residual combining the effect of transient eddies and topographic changes ($\delta(P\text{-}E)_{res}$), (i) and (j) covarying humidity and winds ($\delta(P\text{-}E)_{VQ}$). Left column: δ(P-E) due to Pliocene full forcing conditions estimated with PlioMIP2 MMM. Right column: δ(P-E) due to vegetation and ice sheet changes estimated with CESM2.

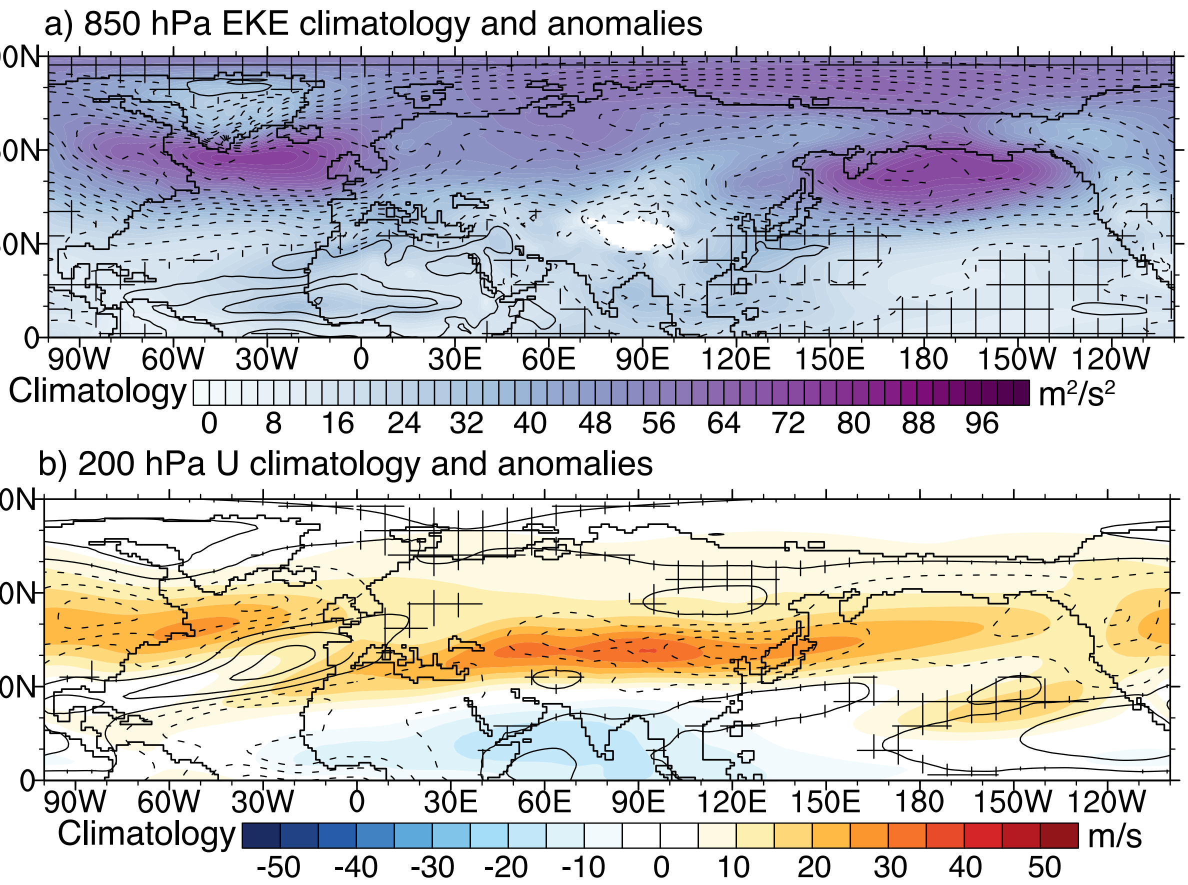

Fig. S6

Climatology of preindustrial (shaded) and changes (contour, dashed: negative; solid: positive) of a) 850 hPa eddy kinetic energy and b) 200 hPa zonal wind between PlioMIP2 and PI averaged for CCSM4, CESM1, and CESM2. Hatches show at least one model with insignificant changes compared to the 100 model year interannual variability through Student's t-test with $p>0.1$.

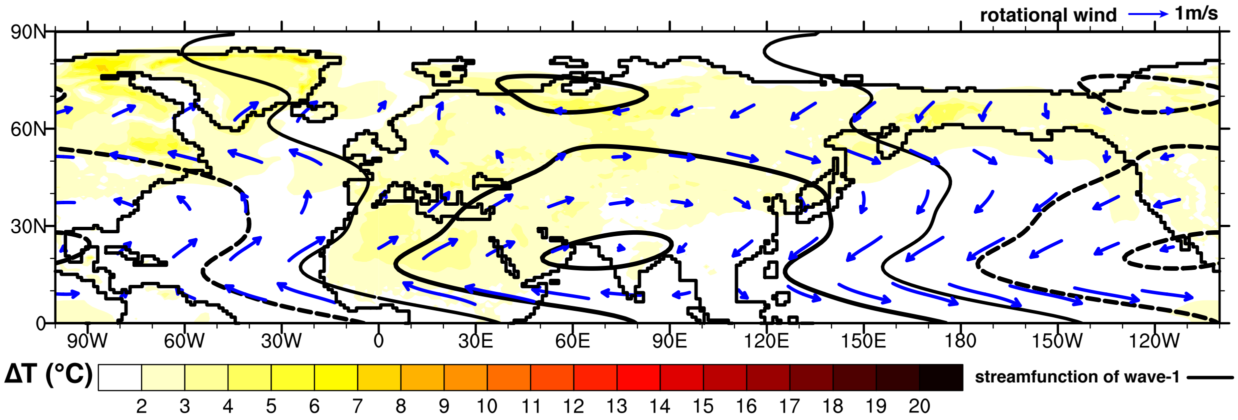

Fig. S7

Changes of surface temperature (color shaded), wave number 1 (contour), and rotational winds (vectors) of stationary wave in response to F_{CO2} simulated by CESM2. Notice that the stationary wave pattern has little dependency on surface temperature changes, but mainly reflects the high-pressure system above Tibet developed during the boreal summer.

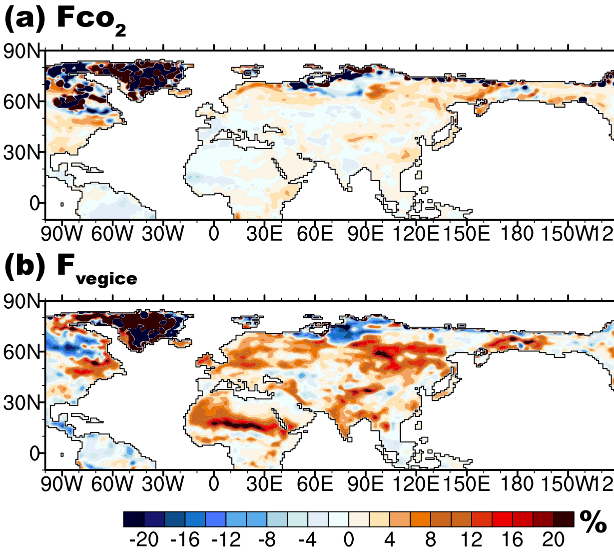

Fig. S8

Change in the % of latent heat flux in total surface heat flux (the sum of latent and sensible heat flux) due to Pliocene (a) CO_2 and (b) vegetation and ice sheet changes.

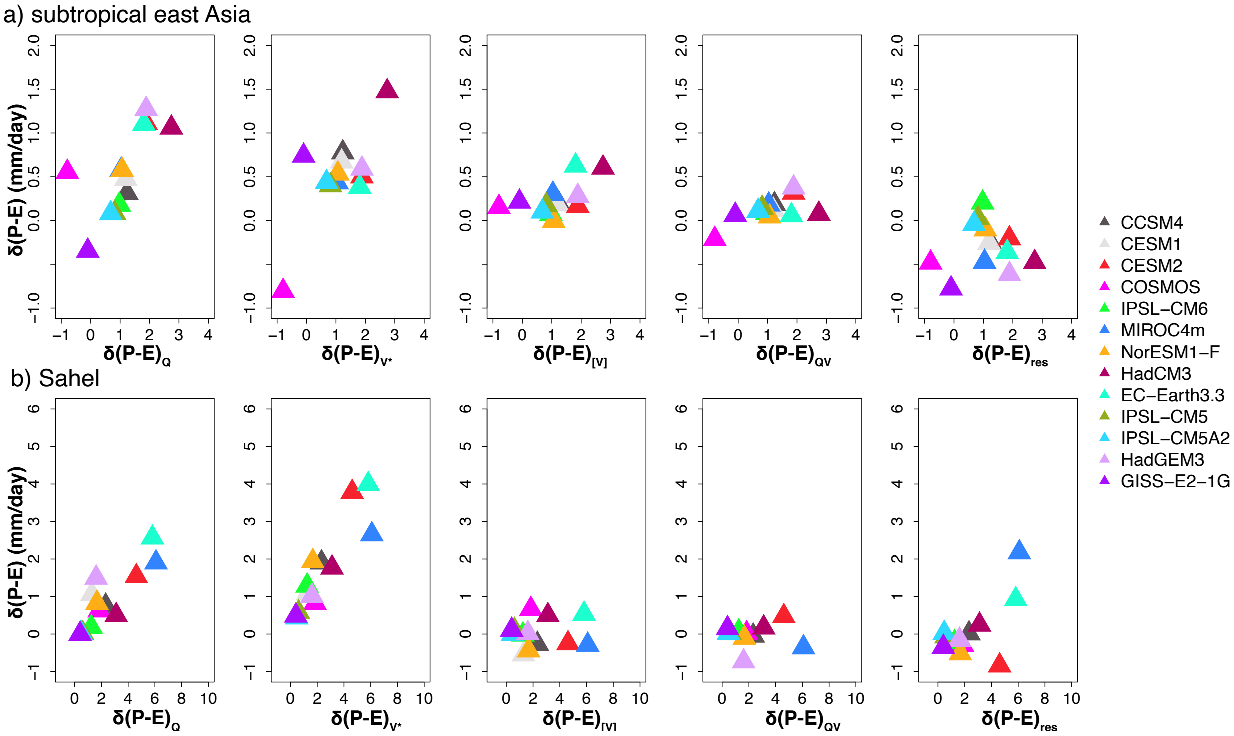

Fig. S9

δ(P-E) across a) Sahel and b) subtropical east Asia (red boxes in Fig. 4) of individual PlioMIP2 simulations as a function of changes in tropospheric humidity (δ(P-E)$_{Q}$), stationary wave dynamics (δ(P-E)$_{V*}$), zonal mean circulation (δ(P-E)$_{[V]}$), non-linear combination of tropospheric humidity and winds (δ(P-E)$_{QV}$), and a residual term (δ(P-E)$_{res}$).

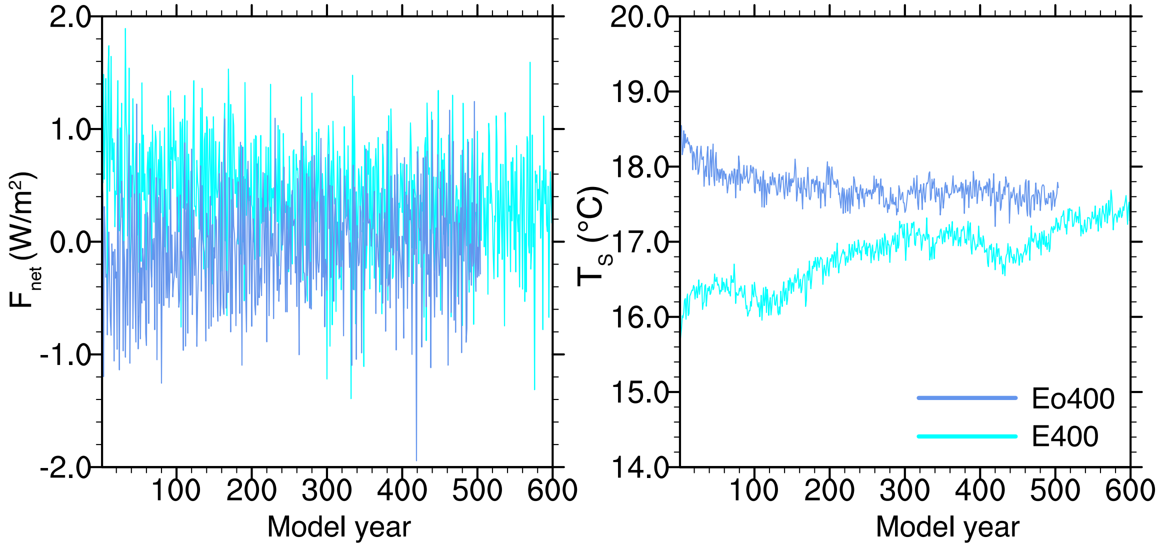

Fig. S10

Time series of global mean net top of the atmosphere radiation imbalance (F_{net}) and surface temperature for the entire simulations of E400 and Eo400.

Data S1. (separate file)

Compilation of Pliocene hydroclimate indicators from published literature.

References

1. M. Hailemichael, J. L. Aronson, S. Savin, M. J. Tevesz, J. G. Carter, δ18O in mollusk shells from Pliocene Lake Hadar and modern Ethiopian lakes: Implications for history of the Ethiopian monsoon. *Palaeogeography, Palaeoclimatology, Palaeoecology*. **186**, 81–99 (2002).

2. C. Contoux *et al.*, Megalake Chad impact on climate and vegetation during the late Pliocene and the mid-Holocene. *Clim. Past*. **9**, 1417–1430 (2013).

3. P. Sanyal, S. K. Bhattacharya, R. Kumar, S. K. Ghosh, S. J. Sangode, Mio–Pliocene monsoonal record from Himalayan foreland basin (Indian Siwalik) and its relation to vegetational change. *Palaeogeography, Palaeoclimatology, Palaeoecology*. **205**, 23–41 (2004).

4. S. Xie *et al.*, Palaeoclimatic estimates for the late Pliocene based on leaf physiognomy from western Yunnan, China. *Turkish Journal of Earth Sciences*. **21**, 251–261 (2012).

5. A. M. Haywood, H. J. Dowsett, A. M. Dolan, Integrating geological archives and climate models for the mid-Pliocene warm period. *Nature Communications*. **7** (2016), doi:10.1038/ncomms10646.

6. E. De La Vega, T. B. Chalk, P. A. Wilson, R. P. Bysani, G. L. Foster, Atmospheric CO 2 during the Mid-Piacenzian Warm Period and the M2 glaciation. *Sci. Rep.* **10**, 1–8 (2020).

7. I. M. Held, B. J. Soden, Robust responses of the hydrological cycle to global warming. *J. Climate* (2006).

8. J. He, B. J. Soden, A re-examination of the projected subtropical precipitation decline. *Nature Climate change*. **7**, 53–57 (2017).

9. C. Chou, J. D. Neelin, Mechanisms limiting the northward extent of the northern summer monsoons over North America, Asia, and Africa. *J. Climate*. **16**, 406–425 (2003).

10. T. Bhattacharya, J. E. Tierney, J. A. Addison, J. W. Murray, Ice-sheet modulation of deglacial North American monsoon intensification. *Nature Geosci*. **11**, 848–852 (2018).

11. J. Scheff, D. M. Frierson, Robust future precipitation declines in CMIP5 largely reflect the poleward expansion of model subtropical dry zones. *Geophys. Res. Lett.* **39** (2012).

12. M. P. Byrne, P. A. O'Gorman, The response of precipitation minus evapotranspiration to climate warming: Why the “wet-get-wetter, dry-get-drier” scaling does not hold over land. *J. Climate*. **28**, 8078–8092 (2015).

13. R. Seager, G. A. Vecchi, Greenhouse warming and the 21st century hydroclimate of southwestern North America. *Proceedings of the National Academy of Sciences*. **107**, 21277–21282 (2010).

14. A. L. Swann, I. Y. Fung, J. C. Chiang, Mid-latitude afforestation shifts general circulation and tropical precipitation. *Proceedings of the National Academy of Sciences*. **109**, 712–716 (2012).

15. A. Berg *et al.*, Land–atmosphere feedbacks amplify aridity increase over land under global warming. *Nature Climate change*. **6**, 869–874 (2016).

16. K. D. Burke *et al.*, Pliocene and Eocene provide best analogs for near-future climates. *Proceedings of the National Academy of Sciences*. **115**, 13288–13293 (2018).

17. J. E. Tierney *et al.*, Past climates inform our future. *Science*. **370** (2020).

18. M. W. Wara, Permanent El Nino-Like Conditions During the Pliocene Warm Period. *Science*. **309**, 758–761 (2005).

19. A. V. Fedorov *et al.*, Patterns and mechanisms of early Pliocene warmth. *Nature*. **496**, 43–49 (2013).

20. Y. G. Zhang, M. Pagani, Z. Liu, A 12-Million-Year Temperature History of the Tropical Pacific Ocean. *Science* (2014).

21. H. L. Ford, A. C. Ravelo, S. Hovan, A deep Eastern Equatorial Pacific thermocline during the early Pliocene warm period. *Earth and Planetary Science Letters* (2012).

22. J. E. Tierney, A. M. Haywood, R. Feng, T. Bhattacharya, B. L. Otto-Bliesner, Pliocene warmth consistent with greenhouse gas forcing. *Geophys. Res. Lett.* (2019).

23. A. Goldner, N. Herold, M. Huber, The challenge of simulating the warmth of the mid-Miocene climatic optimum in CESM1. *Clim. Past*. **10**, 536 (2014).

24. R. Seager *et al.*, Mechanisms of ENSO-forcing of hemispherically symmetric precipitation variability. *Q.J Royal Met. Soc.* **131**, 1501–1527 (2005).

25. C. M. Brierley *et al.*, Greatly Expanded Tropical Warm Pool and Weakened Hadley Circulation in the Early Pliocene. *Science*. **323**, 1714–1718 (2009).

26. A. V. Fedorov, N. J. Burls, K. T. Lawrence, L. C. Peterson, Tightly linked zonal and meridional sea surface temperature gradients over the past five million years. *Nature Geosci*. **8**, 975–980 (2015).

27. Y. Sun, G. Ramstein, C. Contoux, T. Zhou, A comparative study of large-scale atmospheric circulation in the context of a future scenario (RCP4. 5) and past warmth (mid-Pliocene). *Clim. Past*. **9**, 1613–1627 (2013).

28. D. Rind, Latitudinal temperature gradients and climate change. *J. Geophys. Res.* **103**, 5943–5971 (1998).

29. R. Feng, C. J. Poulsen, M. Werner, Tropical circulation intensification and tectonic extension recorded by Neogene terrestrial δ18O records of the western United States. *Geology*. **44**, 971–974 (2016).

30. N. J. Burls, A. V. Fedorov, Wetter subtropics in a warmer world: Contrasting past and future hydrological cycles. *Proceedings of the National Academy of Sciences*. **114**, 12888–12893 (2017).

31. A. Haywood *et al.*, The Pliocene Model Intercomparison project (PlioMIP) phase 2: scientific objectives and experimental design. *Clim. Past*. **12**, 663–675 (2016).

32. H. Dowsett *et al.*, The PRISM4 (mid-Piacenzian) paleoenvironmental reconstruction. *Clim. Past*. **12**, 1519–1538 (2016).

33. A. M. Haywood *et al.*, A return to large-scale features of Pliocene climate: the Pliocene Model Intercomparison Project Phase 2. *Clim. Past* (2020).

34. G. Danabasoglu *et al.*, The Community Earth System Model version 2 (CESM2). *Journal of Advances in Modeling Earth Systems*. **12**, e2019MS001916 (2020).

35. R. Feng, B. L. Otto-Bliesner, E. C. Brady, N. Rosenbloom, Increased Climate Response and Earth System Sensitivity from CCSM4 to CESM2 in mid-Pliocene simulations. *Journal of Advances in Modeling Earth Systems*, e2019MS002033.

36. U. Salzmann, A. M. Haywood, D. J. Lunt, P. J. Valdes, D. J. Hill, A new global biome reconstruction and data-model comparison for the Middle Pliocene. *Global Ecology and Biogeography*. **17**, 432–447 (2008).

37. M. J. Pound, J. Tindall, S. J. Pickering, Late Pliocene lakes and soils: a global data set for the analysis of climate feedbacks in a warmer world. *Climate of the …* (2014).

38. G. Danabasoglu *et al.*, The Community Earth System Model version 2 (CESM2). *Journal of Advances in Modeling Earth Systems* (2019).

39. E. J. Rohling *et al.*, Making sense of palaeoclimate sensitivity. *Nature*. **491**, 683–691 (2012).

40. A. L. Swann, I. Y. Fung, S. Levis, G. B. Bonan, S. C. Doney, Changes in Arctic vegetation amplify high-latitude warming through the greenhouse effect. *Proceedings of the National Academy of Sciences*. **107**, 1295–1300 (2010).

41. R. Seager, N. Henderson, Diagnostic computation of moisture budgets in the ERA-Interim reanalysis with reference to analysis of CMIP-archived atmospheric model data. *J. Climate*. **26**, 7876–7901 (2013).

42. J. P. Peixoto, A. H. Oort, Physics of climate (1992).

43. D. Coumou, J. Lehmann, J. Beckmann, The weakening summer circulation in the Northern Hemisphere mid-latitudes. *Science*. **348**, 324–327 (2015).

44. A. Dai, T. Wigley, Global patterns of ENSO-induced precipitation. *Geophys. Res. Lett.* **27**, 1283–1286 (2000).

45. K. E. Trenberth, D. P. Stepaniak, J. M. Caron, The global monsoon as seen through the divergent atmospheric circulation. *J. Climate*. **13**, 3969–3993 (2000).

46. M. Biasutti, Rainfall trends in the African Sahel: Characteristics, processes, and causes. *Wiley Interdisciplinary Reviews: Climate Change*. **10**, e591 (2019).

47. A. J. Broccoli, K. A. Dahl, R. J. Stouffer, Response of the ITCZ to Northern Hemisphere cooling. *Geophys. Res. Lett.* **33** (2006).

48. D. M. Frierson *et al.*, Contribution of ocean overturning circulation to tropical rainfall peak in the Northern Hemisphere. *Nature Geosci*. **6**, 940 (2013).

49. T. Schneider, T. Bischoff, G. H. Haug, Migrations and dynamics of the intertropical convergence zone. *Nature*. **513**, 45–53 (2014).

50. M. Biasutti *et al.*, Global energetics and local physics as drivers of past, present and future monsoons. *Nature Geosci*. **11**, 392–400 (2018).

51. C. Tabor, B. Otto-Bliesner, Z. Liu, Speleothems of South American and Asian Monsoons Influenced by a Green Sahara. *Geophys. Res. Lett.* **47**, e2020GL089695 (2020).

52. J. G. Charney, Dynamics of deserts and drought in the Sahel. *Q.J Royal Met. Soc.* **101**, 193–202 (1975).

53. M. Claussen *et al.*, Simulation of an abrupt change in Saharan vegetation in the mid-Holocene. *Geophys. Res. Lett.* **26**, 2037–2040 (1999).

54. M. J. Rodwell, B. J. Hoskins, Monsoons and the dynamics of deserts. *Q.J Royal Met. Soc.* **122**, 1385–1404 (1996).

55. R. Alkama, M. Kageyama, G. Ramstein, A sensitivity study to global desertification in cold and warm climates: results from the IPSL OAGCM model. *Clim Dyn*. **38**, 1629–1647 (2012).

56. E. Armstrong, P. Valdes, J. House, J. Singarayer, Investigating the feedbacks between CO 2, vegetation and the AMOC in a coupled climate model. *Clim Dyn*. **53**, 2485–2500 (2019).

57. F. S. Pausata, G. Messori, Q. Zhang, Impacts of dust reduction on the northward expansion of the African monsoon during the Green Sahara period. *Earth and Planetary Science Letters*. **434**, 298–307 (2016).

58. R. O'ishi *et al.*, PMIP4/CMIP6 last interglacial simulations using three different versions of MIROC: importance of vegetation. *Clim. Past*. **17**, 21–36 (2021).

59. M. J. Pound, A. M. Haywood, U. Salzmann, J. B. Riding, Global vegetation dynamics and latitudinal temperature gradients during the Mid to Late Miocene (15.97–5.33 Ma). *Earth-Science Reviews*. **112**, 1–22 (2012).

60. T. Utescher, V. Mosbrugger, Eocene vegetation patterns reconstructed from plant diversity—a global perspective. *Palaeogeography, Palaeoclimatology, Palaeoecology*. **247**, 243–271 (2007).

61. J. K. Caves *et al.*, The Neogene de-greening of Central Asia. *Geology*. **44**, 887–890 (2016).

62. D. J. Lunt *et al.*, Earth system sensitivity inferred from Pliocene modelling and data. *Nature Geosci*. **3**, 60–64 (2009).

63. U. Salzmann, A. M. Haywood, D. J. Lunt, P. J. Valdes, D. J. Hill, A new global biome reconstruction and data-model comparison for the middle Pliocene. *Global Ecology and Biogeography*. **17**, 432–447 (2008).

64. M. J. Pound *et al.*, Late Pliocene lakes and soils: a global data set for the analysis of climate feedbacks in a warmer world. *Clim. Past*. **10**, 167–180 (2014).

65. S. J. Feakins, P. B. Demenocal, T. I. Eglinton, Biomarker records of late Neogene changes in northeast African vegetation. *Geology*. **33**, 977–980 (2005).

66. H. M. Liddy, S. J. Feakins, J. E. Tierney, Cooling and drying in northeast Africa across the Pliocene. *Earth and Planetary Science Letters*. **449**, 430–438 (2016).

67. P. B. Demenocal, Plio-pleistocene African climate. *Science*. **270**, 53–59 (1995).

68. K. L. Gwet, Testing the difference of correlated agreement coefficients for statistical significance. *Educational and Psychological Measurement*. **76**, 609–637 (2016).

69. S. J. Hunter, A. M. Haywood, A. M. Dolan, J. C. Tindall, The HadCM3 contribution to PlioMIP phase 2. *Clim. Past*. **15**, 1691–1713 (2019).

70. C. Stepanek, E. Samakinwa, G. Lohmann, Contribution of the coupled atmosphere–ocean–sea ice–vegetation model COSMOS to the PlioMIP2. *Clim. Past*, 1–72 (2020).

71. Q. Zhang *et al.*, Simulating the mid-Holocene, Last Interglacial and mid-Pliocene climate with EC-Earth3-LR. *Geosci. Model Dev.* **14**, 1147–1169 (2021).

72. W.-L. Chan, A. Abe-Ouchi, PlioMIP2 simulations using the MIROC4m climate model. *Clim. Past*, 1–35 (2020).

73. N. Tan *et al.*, Modeling a modern-like pCO 2 warm period (Marine Isotope Stage KM5c) with two versions of an Institut Pierre Simon Laplace atmosphere–ocean coupled general circulation model. *Clim. Past*. **16**, 1–16 (2020).

74. X. Li, C. Guo, Z. Zhang, O. H. Otterå, R. Zhang, PlioMIP2 simulations with NorESM-L and NorESM1-F. *Clim. Past*. **16**, 183–197 (2020).

75. C. J. Williams *et al.*, Simulation of the mid-Pliocene Warm Period using HadGEM3: Experimental design and results from model-model and model-data comparison. *Clim. Past*, 1–45 (2021).

76. H. Dowsett *et al.*, The PRISM4 (mid-Piacenzian) paleoenvironmental reconstruction. *Clim. Past*. **12**, 1519–1538 (2016).

77. C. M. Brierley, A. V. Fedorov, Comparing the impacts of Miocene–Pliocene changes in inter-ocean gateways on climate: Central American Seaway, Bering Strait, and Indonesia. *Earth and Planetary Science Letters*. **444**, 116–130 (2016).

78. B. L. Otto-Bliesner *et al.*, Amplified North Atlantic warming in the late Pliocene by changes in Arctic gateways. *Geophys. Res. Lett.* **44**, 957–964 (2017).

79. D. J. Hill, The non-analogue nature of Pliocene temperature gradients. *Earth and Planetary Science Letters* (2015).

80. S. Fauquette *et al.*, Climate and biomes in the West Mediterranean area during the Pliocene. *Palaeogeography, Palaeoclimatology, Palaeoecology*. **152**, 15–36 (1999).

81. B. Blavoux, M. Dubar, M. Daniel, Indices isotopiques (13C et 18O) d'un important refroidissement du climat à la fin du Pliocène (formation lacustre de Puimoisson, Alpes-de-Haute-Provence, France): Isotopic indices (13C and 180) of an imponant cooling at the end of the Pliocene (Puimoisson lacustrine formation, Alpes-de-Haute-Provence, France). *Comptes Rendus de l'Académie des Sciences-Series IIA-Earth and Planetary Science*. **329**, 183–188 (1999).

82. J. A. van Dam, Geographic and temporal patterns in the late Neogene (12–3 Ma) aridification of Europe: the use of small mammals as paleoprecipitation proxies. *Palaeogeography, Palaeoclimatology, Palaeoecology*. **238**, 190–218 (2006).

83. B. D. Peter, African climate change and faunal evolution during the Pliocene–Pleistocene. *Earth and Planetary Science Letters*. **220**, 3–24 (2004).

84. P. B. Demenocal, Plio-pleistocene African climate. *Science*. **270**, 53–59 (1995).

85. A. Zazzo *et al.*, Herbivore paleodiet and paleoenvironmental changes in Chad during the Pliocene using stable isotope ratios of tooth enamel carbonate. *Paleobiology*. **26**, 294–309 (2000).

86. N. E. Levin, Environment and climate of early human evolution. *Annu. Rev. Earth Planet. Sci.* **43**, 405–429 (2015).

87. R. L. Lupien *et al.*, Vegetation change in the Baringo Basin, East Africa across the onset of Northern Hemisphere glaciation 3.3–2.6 Ma. *Palaeogeography, Palaeoclimatology, Palaeoecology*, 109426 (2019).

88. C. J. Campisano, C. S. Feibel, Depositional environments and stratigraphic summary of the Pliocene Hadar formation at Hadar, Afar depression, Ethiopia. *The geology of early humans in the Horn of Africa*. **446**, 179–201 (2008).

89. K. S. Westover *et al.*, Diatom paleolimnology of late Pliocene Baringo Basin (Kenya) paleolakes. *Palaeogeography, Palaeoclimatology, Palaeoecology*, 109382 (2019).

90. A. Munoz, J. Ojeda, B. Sanchez-Valverde, Sunspot-like and ENSO/NAO-like periodicities in lacustrinelaminated sediments of the Pliocene Villarroya Basin (La Rioja, Spain). *Journal of Paleolimnology*. **27**, 453–463 (2002).

91. R. V. Heermance *et al.*, Climatic and tectonic controls on sedimentation and erosion during the Pliocene–Quaternary in the Qaidam Basin (China). *Bulletin*. **125**, 833–856 (2013).

92. D.-D. Rousseau, I. Parra, P. Cour, M. Clet, Continental climatic changes in Normandy (France) between 3.3 and 2.3 Myr BP. *Palaeogeography, Palaeoclimatology, Palaeoecology*. **113**, 373–383 (1995).

93. R. Gaur, S. Chopra, Taphonomy, fauna, environment and ecology of upper Sivaliks (Plio-Pleistocene) near Chandigarh, India. *Nature*. **308**, 353–355 (1984).

94. Y. IGARASHI, M. YOSHIDA, H. TABATA, History of vegetation and climate in the Kathmandu Valley. *Proceedings of the Indian National Science Academy, Part A. Physical sciences*. **54**, 550–563 (1988).

95. S. Xie *et al.*, Palaeoclimatic estimates for the late Pliocene based on leaf physiognomy from western Yunnan, China. *Turkish Journal of Earth Sciences*. **21**, 251–261 (2012).

96. J. Wang, Y. J. Wang, Z. C. Liu, J. Q. Li, P. Xi, Cenozoic environmental evolution of the Qaidam Basin and its implications for the uplift of the Tibetan Plateau and the drying of central Asia. *Palaeogeography, Palaeoclimatology, Palaeoecology*. **152**, 37–47 (1999).

97. A. Koutsodendris *et al.*, Late Pliocene vegetation turnover on the NE Tibetan Plateau (Central Asia) triggered by early Northern Hemisphere glaciation. *Global and Planetary Change*. **180**, 117–125 (2019).

98. Y.-F. Yao *et al.*, Monsoon versus uplift in southwestern China–late Pliocene climate in Yuanmou Basin, Yunnan. *PLoS One*. **7**, e37760 (2012).

99. Z. Chang, J. Xiao, L. Lü, H. Yao, Abrupt shifts in the Indian monsoon during the Pliocene marked by high-resolution terrestrial records from the Yuanmou Basin in southwest China. *Journal of Asian Earth Sciences*. **37**, 166–175 (2010).

100. S. Ji, J. Nie, D. O. Breecker, Z. Luo, Y. Song, Intensified aridity in northern China during the middle Piacenzian warm period. *Journal of Asian Earth Sciences*. **147**, 222–225 (2017).

101. Y. Sun, Z. An, S. C. Clemens, J. Bloemendal, J. Vandenberghe, Seven million years of wind and precipitation variability on the Chinese Loess Plateau. *Earth and Planetary Science Letters*. **297**, 525–535 (2010).

102. H. Lu, X. Wang, L. Li, Aeolian sediment evidence that global cooling has driven late Cenozoic stepwise aridification in central Asia. *Geological Society, London, Special Publications*. **342**, 29–44 (2010).

103. P. R. Gent *et al.*, The community climate system model version 4. *J. Climate*. **24**, 4973–4991 (2011).

104. J. W. Hurrell *et al.*, The community earth system model: a framework for collaborative research. *Bull. Amer. Meteor. Soc.* **94**, 1339–1360 (2013).

105. J. H. Jungclaus *et al.*, Ocean circulation and tropical variability in the coupled model ECHAM5/MPI-OM. *J. Climate*. **19**, 3952–3972 (2006).

106. W. Hazeleger *et al.*, EC-Earth V2. 2: description and validation of a new seamless earth system prediction model. *Clim Dyn*. **39**, 2611–2629 (2012).

107. C. Gordon *et al.*, The simulation of SST, sea ice extents and ocean heat transports in a version of the Hadley Centre coupled model without flux adjustments. *Clim Dyn*. **16**, 147–168 (2000).

108. O. Marti *et al.*, Key features of the IPSL ocean atmosphere model and its sensitivity to atmospheric resolution. *Clim Dyn*. **34**, 1–26 (2010).

109. O. Boucher *et al.*, Presentation and evaluation of the IPSL-CM6A-LR climate model. *Journal of Advances in Modeling Earth Systems*. **12**, e2019MS002010 (2020).

110. H. Hasumi, S. Emori, K-1 coupled model (MIROC) description. K-1 Technical Report 1. *Center for Climate System Research, University of Tokyo* (2004).

111. Z. S. Zhang *et al.*, Pre-industrial and mid-Pliocene simulations with NorESM-L. *Geosci. Model Dev.* **5**, 523–533 (2012).

112. H. T. Hewitt *et al.*, Design and implementation of the infrastructure of HadGEM3: The next-generation Met Office climate modelling system. *Geosci. Model Dev.* **4**, 223–253 (2011).

113. M. Kelley *et al.*, GISS-E2. 1: Configurations and climatology. *Journal of Advances in Modeling Earth Systems*. **12**, e2019MS002025 (2020).